AD-A030 268

NWC TP 5844

Dynamics of the Oblique Impact and Ricochet of Nondeforming Spheres Against Thin Plates

by
Marvin E. Backman
and
Stephen A. Finnegan
Research Department

SEPTEMBER 1976

Naval Weapons Center
CHINA LAKE, CALIFORNIA 93555

Naval Weapons Center

AN ACTIVITY OF THE NAVAL MATERIAL COMMAND

R. G. Freeman, III, RAdm., USN ..... Commander

G. L. Hollingsworth ..... Technical Director

FOREWORD

This report summarizes one phase of a continuing research program at the Naval Weapons Center in support of explosive ordnance problems.

These studies were supported by Naval Air Task WF32-353-501, and were conducted by personnel of the Detonation Physics Division.

This report has been prepared for timely presentation of information. Although care has been taken in the preparation of the technical material presented, conclusions drawn are not necessarily final and may be subject to revision.

Released by
E. B. ROYCE, *Head,*
Research Department
17 August 1976

Under authority of
G. L. Hollingsworth
Technical Director

NWC Technical Publication 5844

Published by.....Technical Information Department
Collation.....Cover, 35 leaves
First printing.....160 unnumbered copies

REPORT DOCUMENTATION PAGE

READ INSTRUCTIONS BEFORE COMPLETING FORM

1. REPORT NUMBER: NWC TP 5844	2. GOVT ACCESSION NO.
3. RECIPIENT'S CATALOG NUMBER	
4. TITLE (and Subtitle): DYNAMICS OF THE OBLIQUE IMPACT AND RICOCHET OF NONDEFORMING SPHERES AGAINST THIN PLATES	5. TYPE OF REPORT & PERIOD COVERED: Final
	6. PERFORMING ORG. REPORT NUMBER
7. AUTHOR(s): Marvin E. Backman and Stephen A. Finnegan	8. CONTRACT OR GRANT NUMBER(s)
9. PERFORMING ORGANIZATION NAME AND ADDRESS: Naval Weapons Center, China Lake, California 93555	10. PROGRAM ELEMENT, PROJECT, TASK AREA & WORK UNIT NUMBERS: AIRTASK WF32-353-501
11. CONTROLLING OFFICE NAME AND ADDRESS: Naval Weapons Center, China Lake, California 93555	12. REPORT DATE: September 1976
	13. NUMBER OF PAGES: 68
14. MONITORING AGENCY NAME & ADDRESS (if different from Controlling Office)	15. SECURITY CLASS. (of this report): Unclassified
	15a. DECLASSIFICATION/DOWNGRADING SCHEDULE

16. DISTRIBUTION STATEMENT (of this Report)

Approved for public release; distribution unlimited.

17. DISTRIBUTION STATEMENT (of the abstract entered in Block 20, if different from Report)

18. SUPPLEMENTARY NOTES

19. KEY WORDS (Continue on reverse side if necessary and identify by block number)

Analytical Prediction
Dynamics
Oblique Impact
Perforation
Ricochet
Rigid Body Mechanics

20. ABSTRACT (Continue on reverse side if necessary and identify by block number)

See back of form.

(U) *Dynamics of the Oblique Impact and Ricochet of Nondeforming Spheres Against Thin Plates*, by Marvin E. Backman and Stephen A. Finnegan. China Lake, Calif., Naval Weapons Center, September 1976. 68 pp. (NWC TP 5844, publication UNCLASSIFIED.)

(U) The dynamics of the impact of hard spheres against mild steel and aluminum alloy plates has been investigated by using an analytical model of impact dynamics to interpret experimental data. The analytical model assumes rigid body response of the sphere to forces on the sphere expressed as a quadratic function of the speed of impact and a factor equal to the presented area of contact between the sphere and plate. The dependence of the force on speed is determined by an empirical correlation of the constants in the quadratic function to experimental measurements of the residual speed for impacts at normal incidence. The failure of the plates is modeled by the removal of resisting force over predetermined areas once critical depths of penetration have been exceeded. A scheme for determining the direction of the force on a sphere impacting at oblique incidence, the resolution into a force decelerating the sphere and a force deflecting the sphere, and a prediction of the change in these components due to failure of the plate result in predictions of three kinds of impacts: (1) ricocheting impacts, (2) impacts in which the sphere stops during contact with the plate, and (3) perforations. The shapes of the trajectories are also predicted in each case. Agreement between experimental data and predictions at oblique incidence shows reasonable accuracy in the modeling of the dynamics of impact at oblique incidence. Included in the predictions are specific features of the correlation of residual speed and obliquity with impact speed and obliquity. These features, which are associated with failure of the plate, are supported by experimental data but are not obvious without the predictions.

CONTENTS

INTRODUCTION

This work is part of an investigation with the long-range objective of predicting projectile trajectories and the forces applied to projectiles during impacts against thin plates of moderate hardness at speeds and obliquities typical of current ballistic weapons. The first stage of this investigation is restricted to predicting trajectories and forces in the impact of spheres against thin plates. Spheres are chosen because the symmetry of the sphere simplifies the dynamics of the interaction, thus making it easier to evaluate the procedures used in predicting trajectories and forces.

The predictive procedure consists of analytical and experimental parts. The analytical procedure predicts trajectories and forces from the impact speed, obliquity, radius and mass of the sphere, and empirical constants that characterize the target. Experimental data on impacts at normal incidence are used to determine the empirical constants that are needed in the analytical procedure.

ANALYTICAL PROCEDURE

TYPICAL IMPACT PHENOMENA

The analytical procedure predicts the behavior of an impact system consisting of a very hard sphere and a significantly softer plate. The prediction is made by representing the dynamics of the real system by idealized analytical models of the response of this system to impact. In order to explain the predictive system, the principal phenomena of the impact of a hard sphere against the softer, comparatively thin plate will be described in this section; the following section will present approximations and assumptions that simplify the analytical representation of these phenomena.

When the sphere strikes the plate, several things happen simultaneously: the sphere and the plate begin to deform, stresses develop in both bodies as the result of the deformation, and both bodies are accelerated as the result of the forces on the surface of contact. Interest is here restricted to impacts that leave the sphere intact. Such impacts occur if the sphere is very hard and the plate is much more ductile. Spheres used in this work were of a hard SAE 52100 steel, and the plate was a more ductile SAE 1010 steel or 2024-T3 aluminum alloy. With this system the spheres were recovered intact at impact speeds up to 1.2 km/s.

Those parts of the craters in direct contact with the spheres bore the dimensions and curvature of the spheres, thus demonstrating that the spheres not only maintained their integrity but were deformed very little during impact, while the plates deformed to take the shape of the sphere. Figure 1 is an example of crater cross sections formed by essentially nondeforming spheres.

Observation of crater shape for many impacts shows that the sphere had moved along curved trajectories for all impacts except those at normal obliquity. The craters and high-speed photographs show three distinct final states of motion: ricochet from the front surface of the plate, embedment within the plate, and perforation of the plate. In the perforation mode, the plate fails during impact, making it feasible for the sphere to pass through the plate. Failure may also occur in either an embedding or a ricocheting impact, but it does not influence the interaction enough to change the outcome. The observation of craters formed by oblique impact shows that all such impacts begin with deflections that would lead to ricochet. Embedding impacts are those in which the projectile speed is reduced to zero during the interaction. The reduction to zero velocity could occur during a ricochet phase of the impact or after a perforation phase has begun.

Plate failure at near normal impact obliquities is by plugging, i.e., by separation of a cylindrical-to-truncated conical plug from the plate to form a symmetrical hole through which the projectile ultimately passes (Figure 2). At larger angles of obliquity (roughly, over 30 degrees), the failure process loses its symmetry. At these obliquities perforation failures are different for aluminum and steel. For steel, perforation occurs by the formation of a fingerlike piece from the target by fractures that are cylindrical at one end and with two fractures on each side that are parallel to the direction of motion of the sphere along the surface of the plate. This finger bends away from the plate and frequently breaks off. When it breaks, the last point of failure is at the hinge point of its bending (Figure 3a). Failures that lead to perforation in aluminum are markedly different, especially for thin plates. Failures in thin aluminum plates are of a petaling type. A central fracture occurs along the direction of travel of the sphere, and additional fractures travel out from the central fracture forming petals that peel back from the center (Figure 3b).

RESTRICTIONS ON THE IMPACT SYSTEM AND APPROXIMATIONS

The analytical procedure used to represent the sphere-plate system during impact is based on a number of simplifying restrictions and approximations to the observed behavior of the system.

First it is assumed that the analytical procedure can be projectile-oriented and can represent the behavior of the sphere-plate system exclusively in terms of the effect on the motion of the sphere. Figure 4,

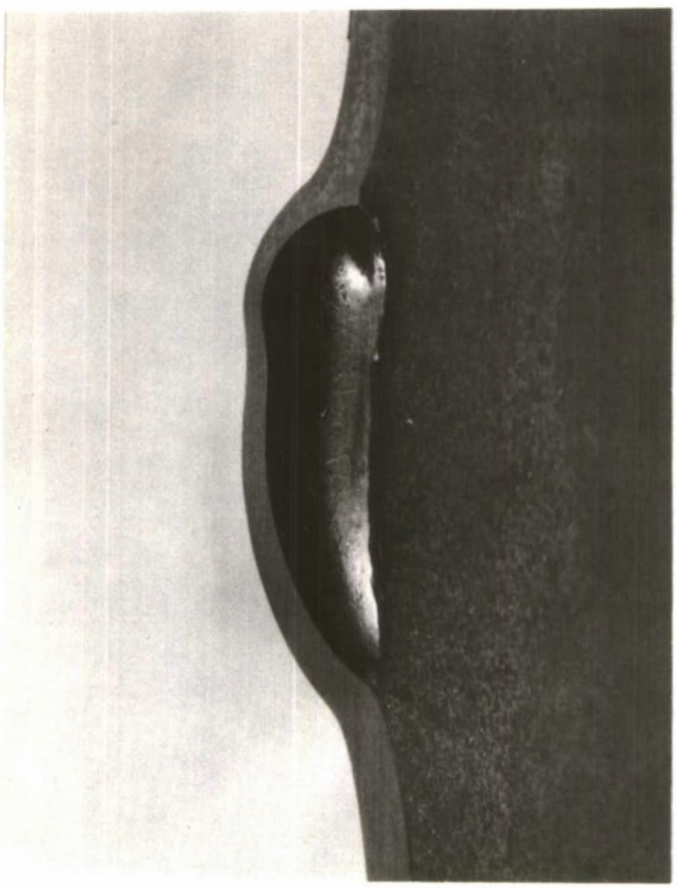

FIGURE 1. Crater Formed by a Sphere That Remained Intact. Sphere: SAE 52100 steel, 6.35 mm in diameter; plate: SAE 1010 steel, 1.47 mm thick.

which illustrates the application of the procedure to a ricochet and a perforation trajectory, helps to explain the role of restrictions and approximations in the analytical procedure. Thus, both for a ricochet (Figure 4a) and for a perforation (Figure 4b), the trajectories, which are indicated by the curves, are calculated by rigid-body response of the sphere to forces exerted on the sphere by the deforming plate. The deformations of the plate will not be explicitly determined, and it is assumed that displacements of the plate material are such as to accommodate to the motion and shape of the sphere. In this process of deformation the plate exerts a force on the sphere that depends on the motion of the projectile relative to the plate and on the extent of contact between the sphere and the plate. This point of view is permitted in part by the restriction on the system that the plate and its supporting structure are much larger and more massive than the sphere, so that

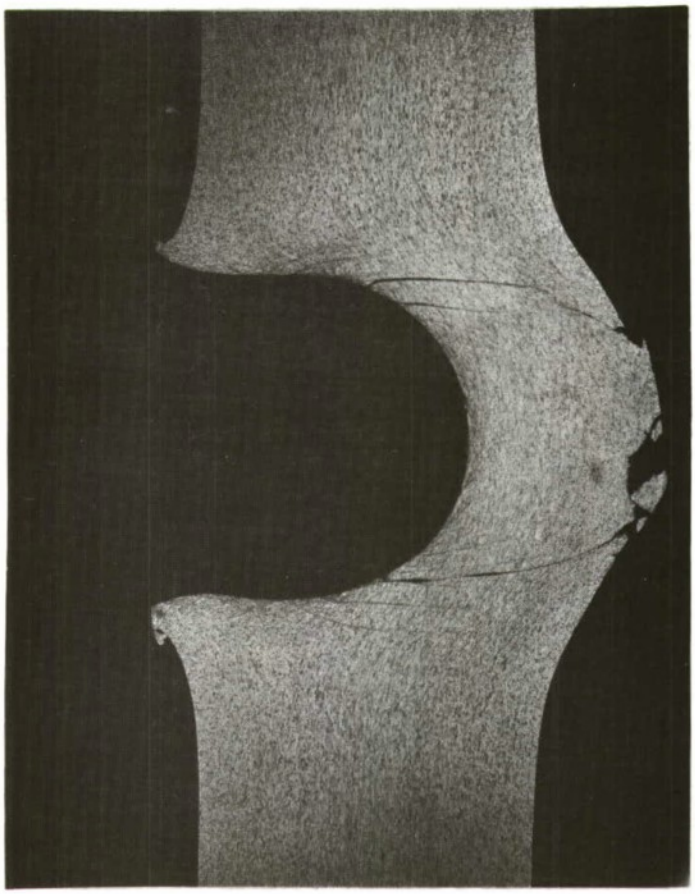

FIGURE 2. Cross Section of a Crater That Displays Plugging-Mode Failure. Sphere: SAE 52100 steel, 6.35 mm in diameter; plate: 2024-T3 aluminum alloy, 6.35 mm thick.

the overall motion of the plate is not significant and the interaction of the plate and the sphere is highly localized about the region of contact. Still another restriction on the system that justifies a completely projectile-oriented point of view is that the plate material is significantly softer than the projectile.

The simultaneous and interrelated processes of deformation, force development, and changes in motion of the sphere are represented in simplified form by approximation of the real trajectory of the sphere by a trajectory composed of segments having constant speed and curvature. These segments correspond to a finite number of calculations concerning location of the sphere, force on the sphere, and change in its state of motion. Figure 4 illustrates ricochet and perforation trajectories that are each approximated by segments of constant speed and curvature. The

(a)

(b)

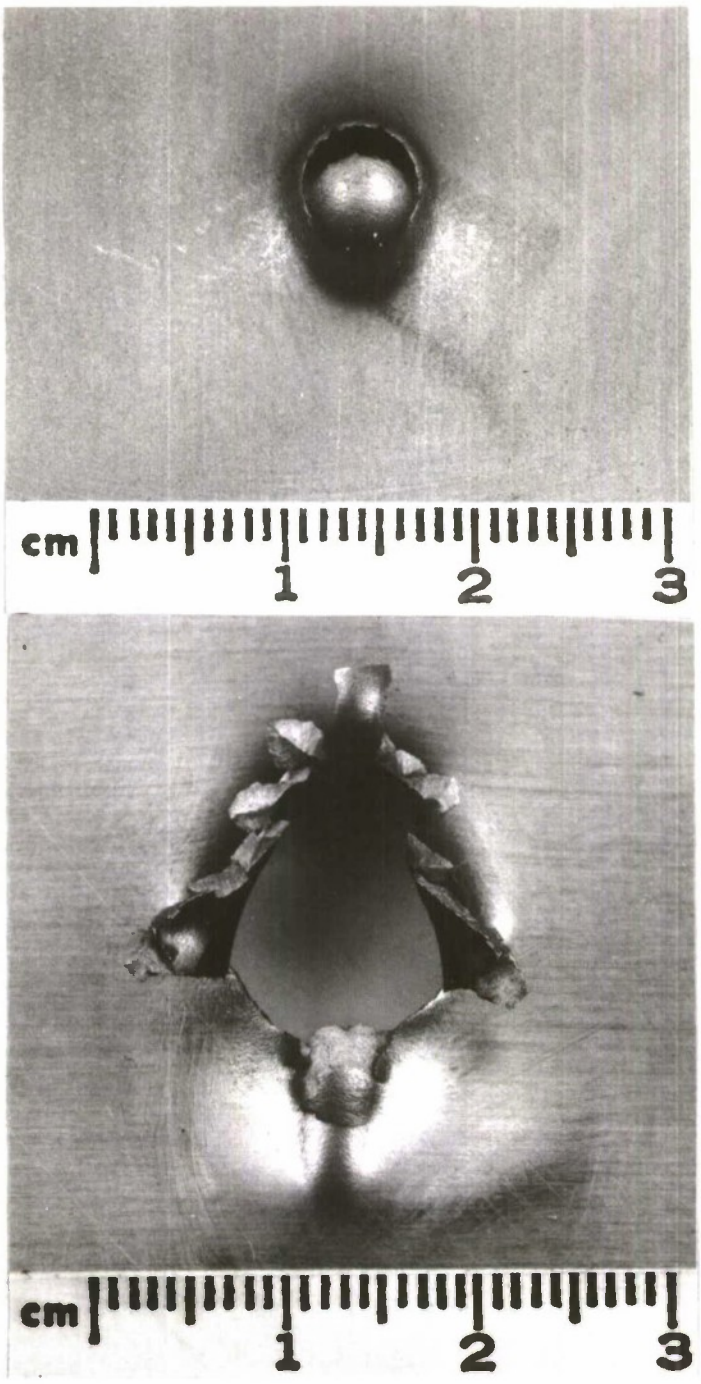

FIGURE 3. Exit-Surface Photographs of Two Craters Formed by Impact of a 6.35-mm SAE 52100 Steel Sphere at Obliquity, Displaying (a) Hinge-Mode Failure of a 1.47-mm SAE 1010 Steel Plate, and (b) Petaling-Mode Failure of a 1.27-mm 2024-T3 Aluminum Alloy Plate.

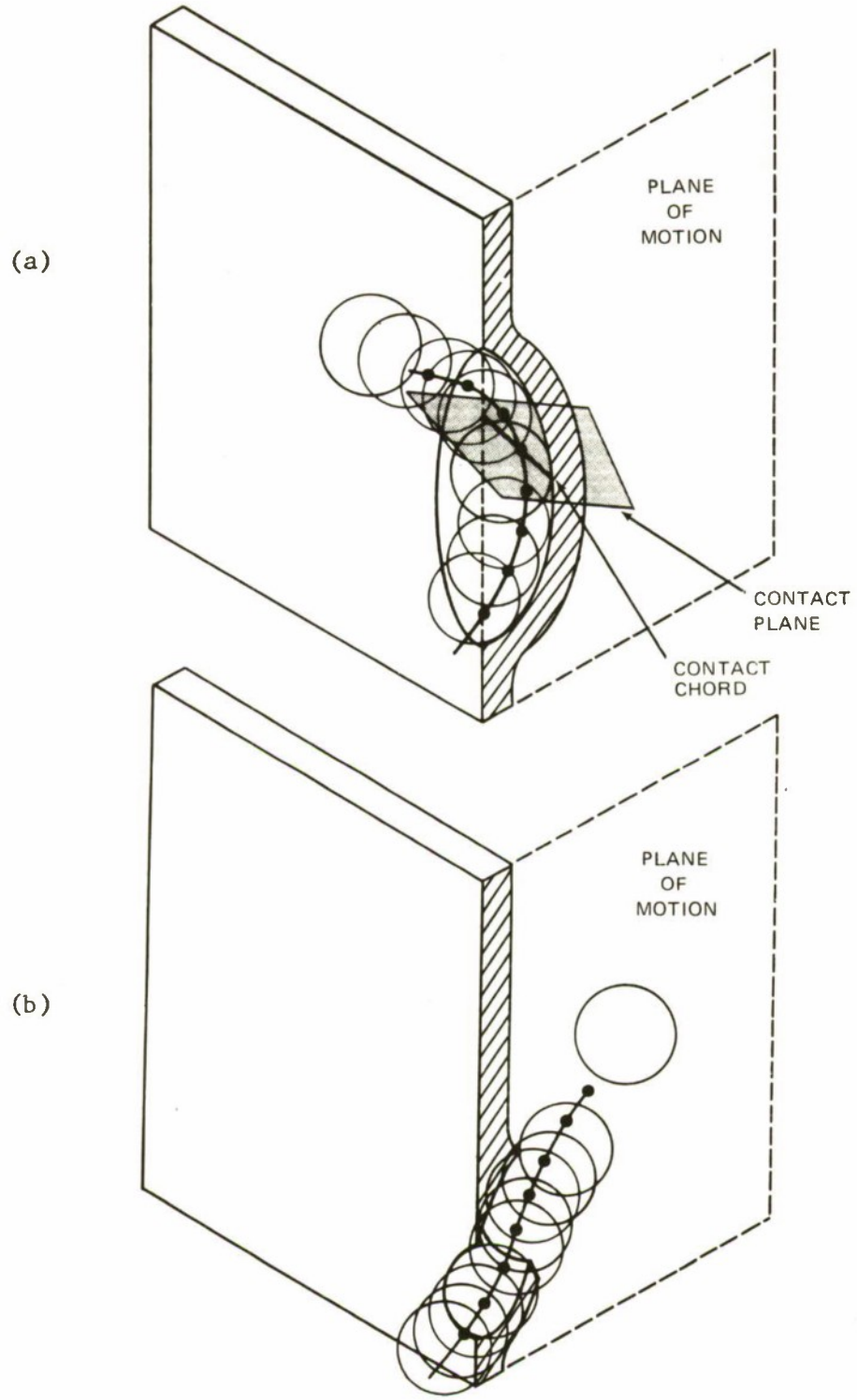

FIGURE 4. Hypothetical Trajectories Illustrating the Application of the Analytical Procedure to (a) Ricochet and (b) Perforation.

basic calculations of the analytical procedure are carried out at the points designated by the heavy dots.

In the present analytical procedure there is no explicit attempt to do detailed calculations of the strain in the plate, to correlate deformation directly with stress, or to integrate surface stresses and tractions into a resultant force. All these processes are implicit in the estimation of the force resisting penetration by an equation of the Poncelet form $F = A(a + bV^2)$ where F is the resisting force, A is the presented area, V is the impact speed, and a and b are constants that characterize the target. The dependence of the force on deformation is expressed through the presented-area factor, and the dependence on speed is given by the quadratic relation. The properties of the system are expressed through constants a and b. The resisting function given above has been used in many investigations of impact at normal incidence.[1-3]

These investigations have shown that this function is capable of predicting the outcome of impacts for a specific system with reasonable accuracy. Typically, the force for any degree of embedment is estimated by this empirical expression, using the intersection of the front surface of the plate and the surface of the sphere as the presented area.

In order to determine the motion of the sphere at oblique impacts, some rule must be made as to how the direction of the force is to be determined from the geometry of the contact between the sphere and the plate. The initial motion of the sphere is in the plane defined by the initial line of flight and the normal to the plate. The force vector that governs the motion after contact is in this plane because of the symmetry of the contact surface about this plane. The rule used for determining the direction of the force within this plane is that the force is normal to the chord connecting the upper and lower extremities of the contact surface and in the plane of motion. This chord will be called the *contact chord*, and the plane that passes through the line of chord and is perpendicular to the plane of motion will be called the *contact plane*. The presented area of the contact surface will be the projection of the contact surface on this plane.

The force on the sphere is considered to be applied to the center of mass of the sphere in accordance with the principles of rigid-body mechanics. In general, there must be a torque applied at the center of mass so that the force system at the center of mass is equivalent to the

---

[1] F. Helie. *Traite de Balestique Experimentale*. Paris, Dumaine, 1884.

[2] Ballistics Institute. *Theory of Armor Piercing* by H. Richter. St.-Louis, France, BI, May 1946. (Report No. 3/46.)

[3] J. Nishiwaki. "Resistance to Penetration of a Bullet Through an Aluminum Plate," *J. Phys. Soc. Jap.*, Vol. 6 (1951), p. 374.

force system applied at the contact surface. In the present procedure any torque of this sort is neglected on the assumption that the resulting rotation and angular momentum of the sphere have no important effect on the interaction. The force at the center of mass is resolved into a force component in the direction of motion and a force component perpendicular to the direction of motion. These components are called the drag force component and the lift force component, respectively, using terminology analogous to that of aerodynamics.

At some point of penetration, the plate fails. For any given calculation this can be assigned a critical penetration, P^*, and it is assumed in the analytical procedure that for any system there is a single critical penetration for failure no matter what the obliquity or impact velocity. It is further assumed that the only important effect of failure is to relieve the force resisting penetration over some designated part of the contact surface. The extent of the relieved section is given by an angle α^* that is measured from the normal to the plate as shown in Figure 5. The effect of failure on the trajectory of the sphere is then automatically taken into account by the model of the dynamics of the sphere.

DETAILS OF THE ANALYTICAL PROCEDURE

This section summarizes the principal steps and equations that are used to predict the results of impact. This prediction procedure requires as input data the mass, m, of the sphere; its radius, R_s; its impact speed, V_s; the obliquity, θ_s; the thickness of the plate, T; and the constants, a and b, that characterize the target plate. The actual trajectory of the sphere is approximated by a finite number of segments, each having a constant curvature and constant speed along its length. The segment represents the displacement of the sphere for a known time interval, dt. For each segment the main steps of the analytical procedure are as follows:

1. The force on the sphere is calculated at the beginning of each segment by the empirical equation and with direction normal to the contact plane.

2. The force is resolved into a drag component that is in the direction of motion and a lift component that is in the direction perpendicular to the motion of the sphere.

3. The change in speed of the sphere during a time, dt, is calculated from the drag component of force, and the curvature of the path is calculated from the lift component of force.

4. The change in the position of the sphere for the next interval of time, dt, is calculated from the new values for speed and curvature.

5. The penetration of the sphere is compared with the critical penetration for failure to determine whether the plate has failed or is intact.

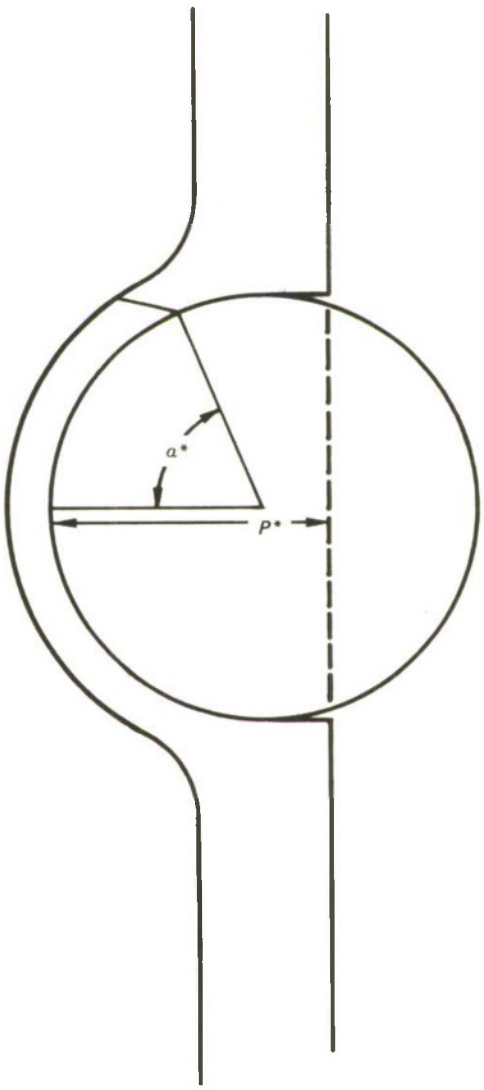

FIGURE 5. Diagram of the Model of Failure by Plugging.

Force on the Sphere Before Plate Failure

The force resisting penetration is given by the equation

$$F = A(a + bV^2 \cos^2 \psi) \tag{1}$$

where F is the resisting force, A is the presented area, V is the speed, a and b are constants that characterize the target plate, and ψ is the angle between the sphere's line of flight and the normal to the contact surface (Figure 6).

A general expression for the presented area, A, is

$$A = \frac{R_e^2}{2}(\Gamma_e - \sin \Gamma_e) \cos \phi + \frac{R_s^2}{2}(\Gamma_s - \sin \Gamma_s) \cos (\theta - \phi) \tag{2}$$

where R_e is the radius of embedment,

$$R_e = (2R_s P - P^2)^{1/2} \tag{3}$$

the angle Γ_e is

$$\Gamma_e = 2\pi - 2 \cos^{-1}[(R_s - P)/(R_e \tan \theta)] \tag{4}$$

and when

$$(R_s - P)/\tan \theta > R_e, \text{ then } \Gamma_e = 2\pi$$

The angle Γ_s is

$$\Gamma_s = 2 \cos^{-1}[(R_s - P)/(R_s \sin \theta)] \tag{5}$$

and when

$$(R_s - P)/\sin \theta > R_s, \text{ then } \Gamma_s = 0$$

The direction of the force is specified as normal to the contact plane; thus, the force is at an angle, ϕ, with respect to the normal to the plate. This angle is defined in terms of the obliquity, θ, and the penetration, P, as

$$\phi = \frac{\theta + \sin^{-1}(P - R_s)/R_s}{2} \tag{6}$$

and this angle must lie between zero and θ.

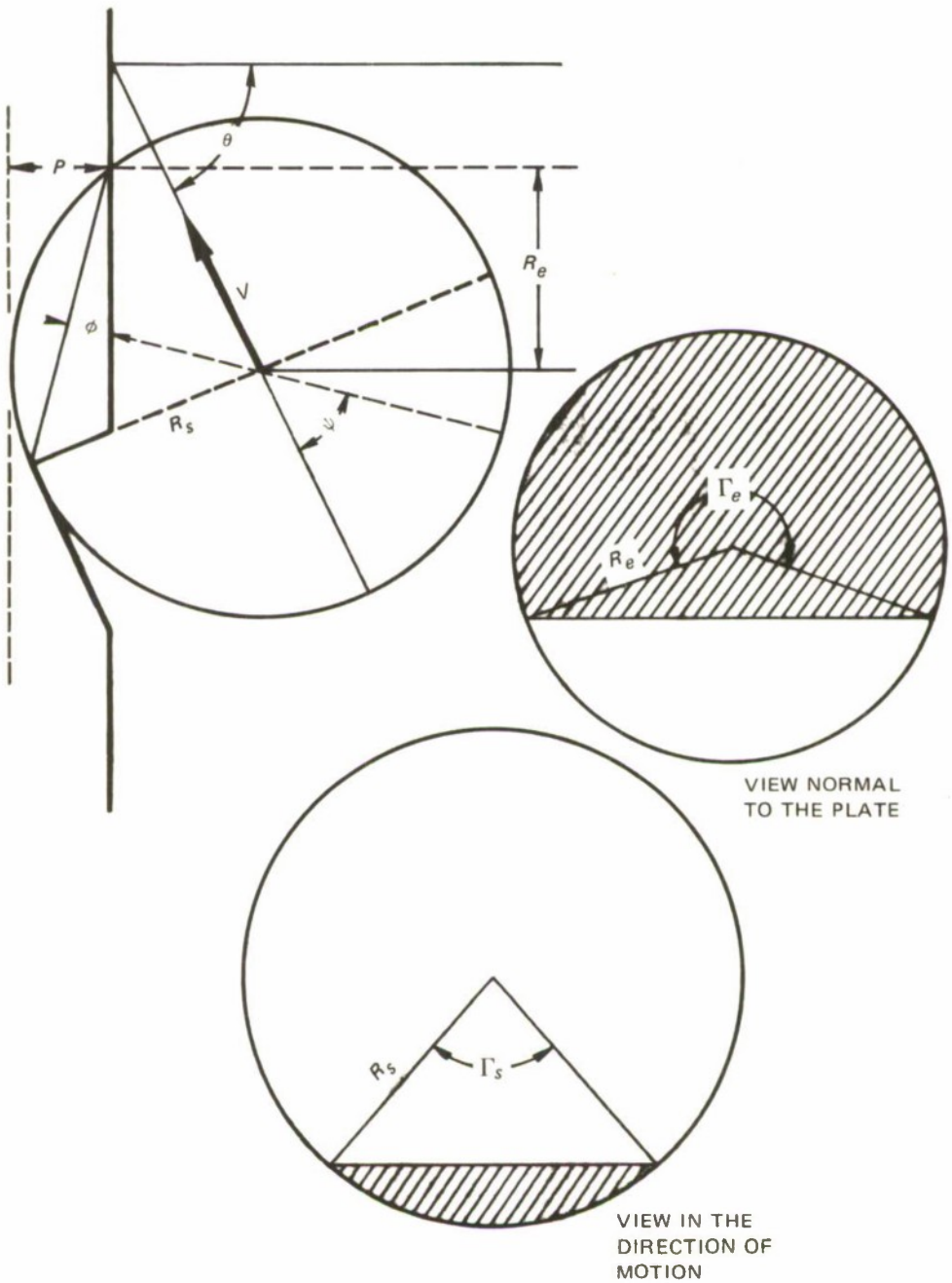

FIGURE 6. Diagram of the Forces on a Sphere. Shaded areas are projected contact surfaces.

Model of Failure of the Plate

For impacts at normal incidence the failure is symmetrical, and a plug is immediately expelled from the plate. Plugging failure is put in the analytical model by a penetration criterion that determines the onset of failure. The expulsion of the plug is represented by the immediate removal of resisting force over the region of the plate defined by the angle α^*. Failure of the plate for impacts at oblique incidence becomes increasingly asymmetrical with increasing obliquity, and plate fractures result in a petaling formation as the projectile penetrates into the plate.

The model of failure of the plate for impacts at obliquity consists of the following elements: (1) a critical penetration, P^*, for the onset of failure; (2) an angle, α^*, to define the initial location at which failure occurs; and (3) a model of the development of failure as the sphere continues its motion. There are two options here: (1) to relieve resistance immediately as for normal incidence, and (2) to maintain contact over a decreasing contact surface so as to model the peelback of a "hinge."

Elements of the model of failure are illustrated for oblique incidence in Figure 7. In Figure 7a the sphere has reached the distance P^* at which failure occurs. The location of the failure on the sphere is given by the angle, α^*, which is measured with respect to the normal to the exit surface of the plate, so that the specification of the location of failure is with respect to the plate orientation. In the first option resistance is relieved over all of the contact surface up to the angle α^*. In Figure 7B the sphere has continued its trajectory, and the difference between angles α_2 and α_1 defines the opening of the failure. These angles are computed on the premise that the lengths of the plate elements in contact with the sphere remain invariant above and below the failure as the sphere moves and the failure opens up. This is done by keeping the angle Ω constant for the upper segment and by reducing the lower segment by a length increment, dS', for an increment of motion, dS, and change of obliquity, $d\theta$, that is given by

$$dS' = dS + R_s d\theta \tag{7}$$

where $R_s d\theta$ is the swing of the radius of the sphere through the increment of obliquity, $d\theta$.

Force on the Sphere After Plate Failure

After the plate has failed, the calculation of force has to account for relief of the force over part of the plate due either to plugging or petaling. For symmetrical failure by plugging, the removed part of the plate is defined by the intersection of the spherical surface by a plane

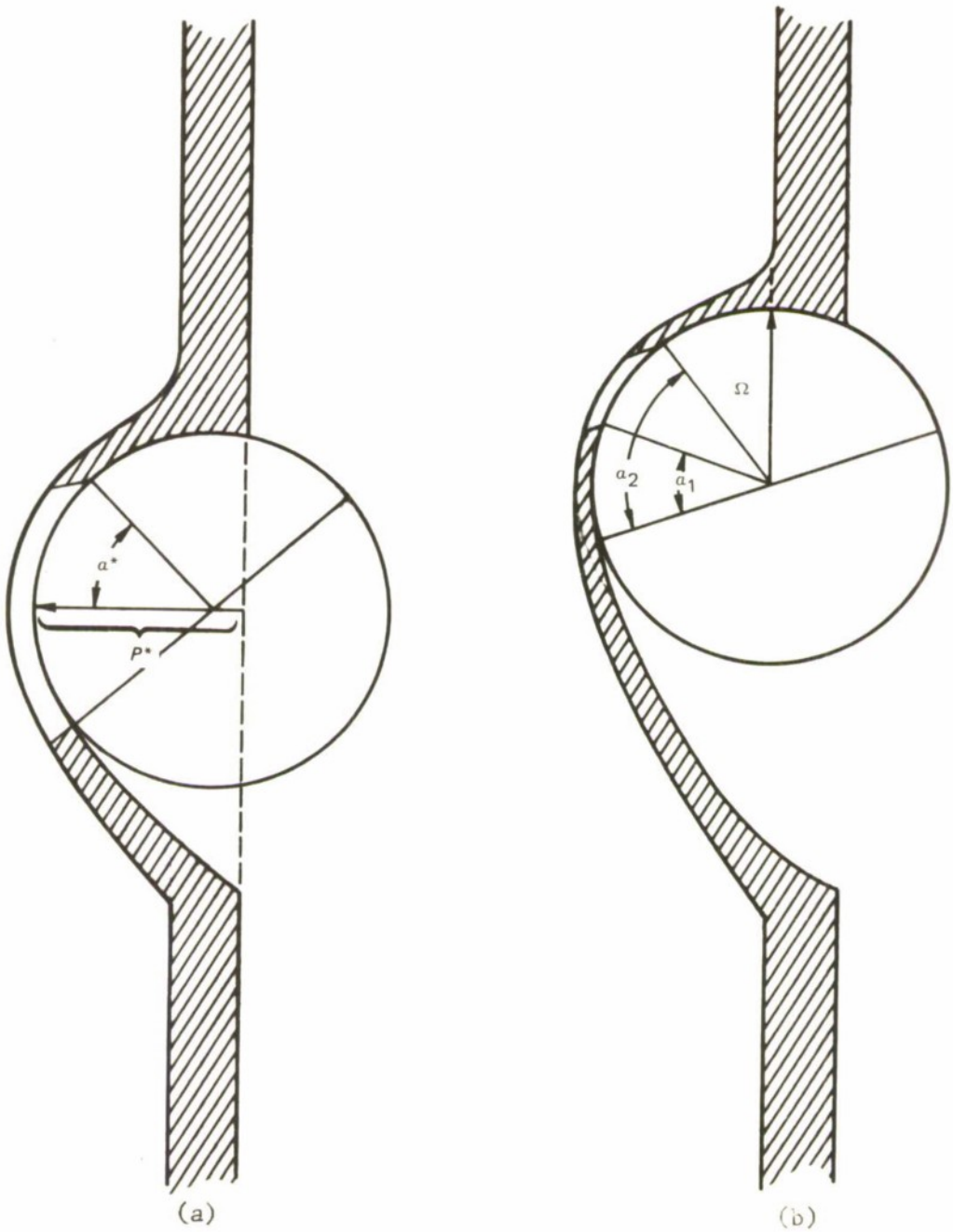

FIGURE 7. Diagram of the Hinge Mode of Failure.

that is parallel to the front surface of the plate and displaced from it by a distance, h, that is related to the penetration and angle α by the equation

$$h = R_s \cos \alpha + P - R_s \tag{8}$$

Procedures for determining the presented area and the inclination of the contact surface are identical to those used for the calculation of force before the failure of the plate (Equations 1 through 6), except that the plane of reference is displayed by the distance h (Figure 8). The equations for the presented area are

$$A' = \frac{R'^2_e}{2} (\Gamma'_e - \sin \Gamma'_e) \cos \phi' + \frac{R_b^2}{2} (\Gamma'_s - \sin \Gamma'_s) \cos (\theta - \phi') \tag{9}$$

$$R'_e = [2R_s(P - h) - (P - h)^2]^{1/2} \tag{10}$$

where

$$\Gamma'_e = 2\pi - 2 \cos^{-1} [(R_s - P + h)/(R'_e \tan \theta)] \tag{11}$$

$$\Gamma'_s = 2 \cos^{-1} [(R_s - P + h)/(R_s \sin \theta)] \tag{12}$$

and for inclination of the contact plane,

$$\phi' = \frac{\theta + \sin^{-1}(P - h - R_s)/R_s}{2} \tag{13}$$

The force calculated for this area is

$$F' = A'(a + bV^2 \cos^2 \psi) \tag{14}$$

Let F^* be the same as F of Equation 1; then the net force, F, acting on the sphere after plugging failure is the force F^* calculated without plate failure minus the force F', the force relieved by the plugging failure; i.e.,

$$F = F^* - F' \tag{15}$$

The analytical model of the hinge mode of failure uses the relieving effect of the plugging model but in addition includes the resistance due to the finger that is formed by the unsymmetrical failure characteristic of oblique impact. This resistance is calculated as

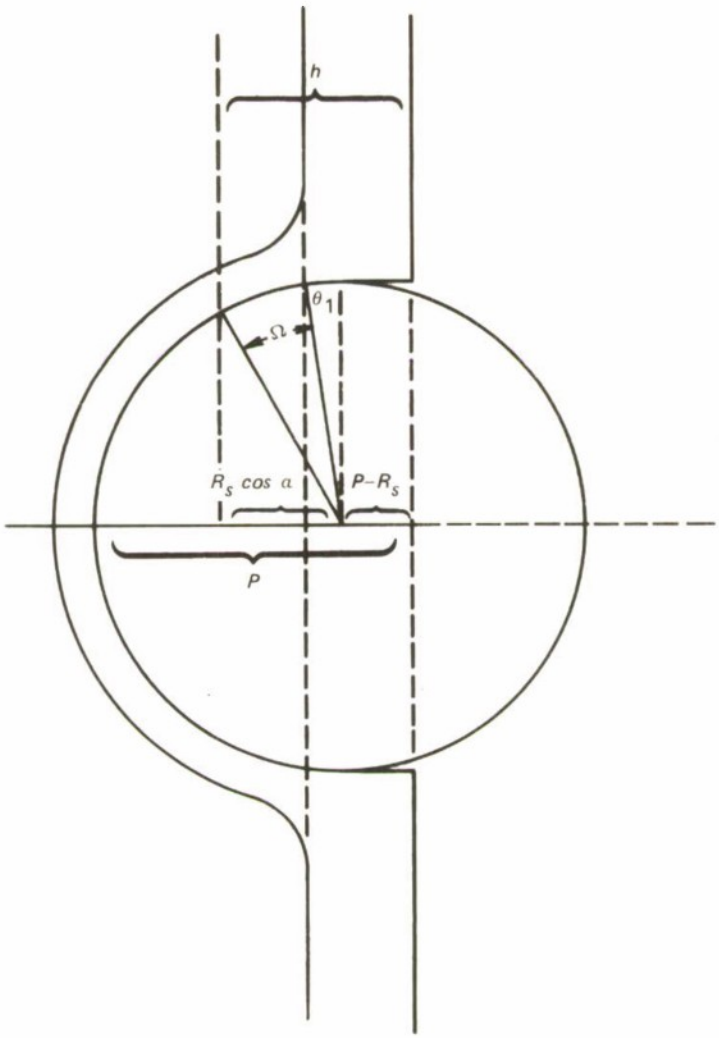

FIGURE 8. Diagram of the Forces on a Sphere After Plate Failure.

$$F'' = A_s(a + bV^2 \cos^2 \psi) \tag{16}$$

where

$$A_s = \pi[R_s \sin (\beta/2)]^2 \tag{17}$$

and β is the angle between the upper edge of the hinge and the last point of contact with the sphere, as shown in Figure 9. This angle begins with the value $\beta = \alpha + 90° - \theta$ if this value is less than 2α; if not, then $\beta = 2\alpha$ until θ is greater than θ_1. For each segment of the path thereafter, the value of β is corrected for the displacement of the segment by

$$\beta' = \beta - d\theta - (dS/R_s) \tag{18}$$

The angle ψ' is calculated by

$$\psi' = 90° + \theta - \theta_1 - (\beta/2) \tag{19}$$

if $\theta - \theta_1$ is negative, and by

$$\psi' = 90° - (\beta/2) \tag{20}$$

if the difference is positive.

The net force under conditions of hinge failure is

$$F = F* - F' + F'' \tag{21}$$

Dynamics and Kinematics of the System

The dynamics of the impact of the sphere against the plate are modeled by calculating the force on the sphere by the method just described and then calculating the rigid-body response of the sphere to this force. It is convenient to resolve the force into a component that is in the current direction of motion and a component that is perpendicular to the current direction of motion. Changes in the speed of the sphere are calculated from the component that is in the direction of motion, and the curvature of the trajectory is calculated from the component perpendicular to the direction of motion.

The force calculated by Equations 1, 15, or 21 is at an angle, ψ, with respect to the direction of motion of the sphere. This angle can

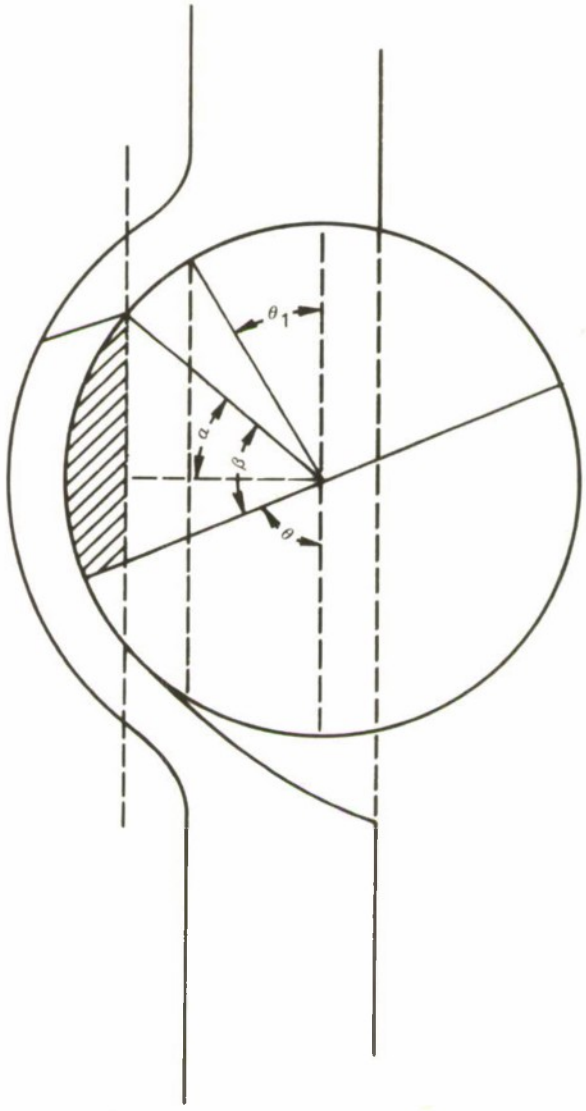

FIGURE 9. Diagram of the Parameters of Hinge Failure.

be determined from the obliquity, θ, and the inclination of the contact plane, ϕ:

$$\psi = \theta - \phi \tag{22}$$

The drag and lift components of the force are then

$$F_D = F \cos \psi \tag{23}$$

$$F_L = F \sin \psi \tag{24}$$

The changes in velocity and the curvature of the trajectory corresponding to these components of force are

$$dV = F_D dt/m \tag{25}$$

and

$$r = mV^2/F_L \tag{26}$$

where dt is the increment of time over which the calculation is carried out, and r is the radius of curvature of the trajectory.

These quantities, dV and r, determine the segments of the trajectories. The obliquity is changed as

$$d\theta = Vdt/r \tag{27}$$

so that the new obliquity is θ',

$$\theta' = \theta + d\theta \tag{28}$$

and the corresponding increment of penetration is

$$dP = V \cos \theta dt \qquad P' = P + dP \tag{29}$$

and the corresponding increment of lateral motion is

$$dY = V \sin \theta dt \qquad Y' = Y + dY \tag{30}$$

These steps are illustrated in Figure 10, where it should be noted that segment size is exaggerated to facilitate the explanation.

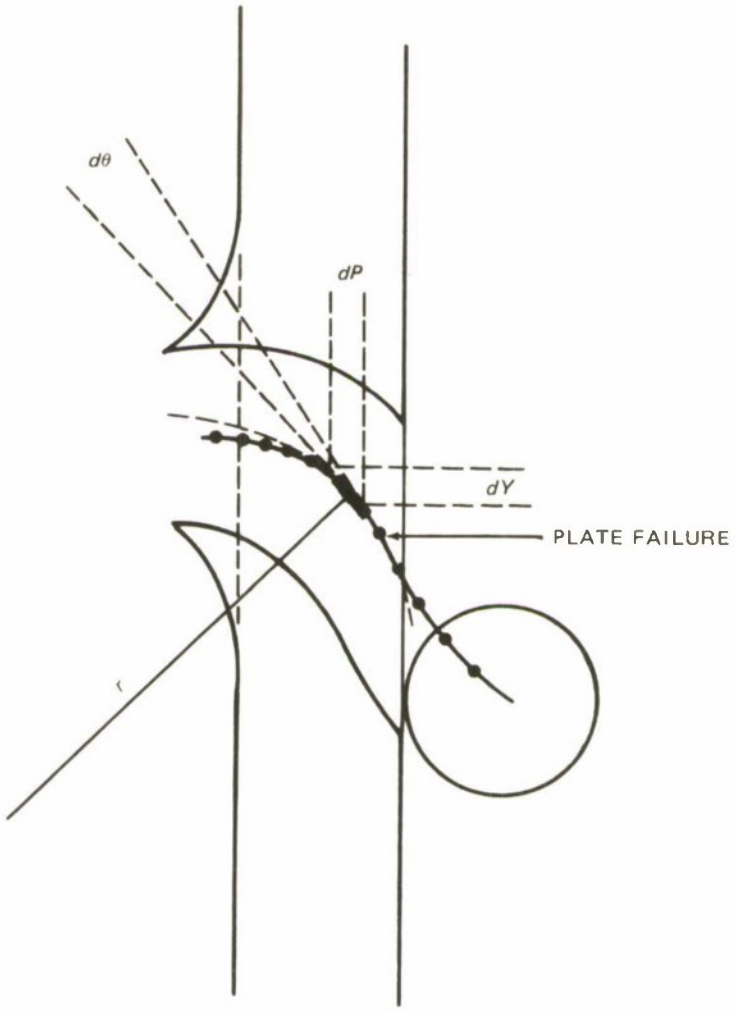

FIGURE 10. Diagram of the Kinematics of Trajectories.

Prediction of Crater Shape

The sphere sweeps out a tube as it moves along its trajectory. The crater in the plate is the part of the volume of the tube extending beyond the front surface of the plate. The shape of the crater is specified completely by its cross section in the plane of motion of the sphere; thus, crater shapes can be calculated from trajectories as the projection on the X,Y plane of the tube intersection that is swept out by the sphere, and the half space defined by the plane of the front surface of the plate. The projection of the tube is two curves. The curve corresponding to the side of the projection defining the crater shape is determined from the trajectory as the focus of points given by

$$x = X + R_s \sin \theta \tag{31}$$

$$y = Y - R_s \cos \theta \tag{32}$$

where x and y are points on the projection of the tube, X and Y are points on the trajectory, and R_s and θ are, respectively, the radius of the sphere and the obliquity of the motion of the sphere at a given point on its trajectory. The intersection of this curve with the half space defined by the front surface of the plate is the curve that describes the crater shape.

It is a minor convenience to define x and y for each calculation in such a way that x and y are both zero at the entry intersection of the crater shape curve with the front surface of the plate. Trajectories are arbitrarily defined to have initial values

$$X = -R_s \tag{33}$$

$$Y = 0 \tag{34}$$

The corresponding values of x and y are

$$x = -R_s + R_s \sin \theta$$

$$y = -R_s \cos \theta \tag{36}$$

In general, y will not be zero when x is zero. A set of coordinates x', y' such that the entry intersection at the front surface of the plate is given by $x' = 0$ and $y' = 0$ is determined in our finite step procedure by the simple transformation

$$x' = x \tag{37}$$

$$y' = y + y_o \tag{38}$$

where y_o is determined from y_1, the y value corresponding to x_1, the value of x that is positive, by the equation

$$y_o = y_1 - x_1 \tan \theta \tag{39}$$

EXPERIMENTAL DETERMINATION OF EMPIRICAL CONSTANTS

The analytical model requires the mass and radius of the sphere and the thickness of the plate as basic parameters to define the size, configuration, and relevant inertial properties of the system. In addition, the model requires four empirical parameters that account for mechanical properties of the plate. The constants a and b of the force equations represent the capacity of the plate to exert force on the sphere as the plate deforms. The parameter P^* determines the beginning of failure, and the parameter α^* its location. These four parameters must be determined either by separate theoretical considerations or empirically. In the present work these are determined empirically.

The parameters P^* and α^* can be estimated directly from observations on impact craters. A series of observations on impacts with increasing impact speed shows that failure occurs near a constant value of penetration. When failure does occur, it is possible to fix the location on the surface of the sphere and estimate the angle α^*. Such observations on craters are basically consistent with our assumption that failure can be described by assigning constant values of P^* and α^*. However, there are observable variations in these parameters as the speed and obliquity are varied, so that constancy of these parameters as a description of failure is, at best, a good approximation. For example, there are indications that the angle α^* tends to decrease with increasing impact speed, and although the penetration P^* appears to be quite constant for aluminum, it varies considerably for mild steel.

Constants P^* and α^* are selected to match observations of crater formation at normal incidence; then the constants a and b, which characterize the target, are derived from experimental data in a two-step procedure. A statistical procedure operates on experimental data on the residual speed as a function of the impact speed at normal incidence to determine the best values of the constants R and V_o in the DRI equation[4]

$$V_x = R \sqrt{V_s^2 - V_o^2} \tag{40}$$

---

[4] R. Recht and T. W. Ipson. "Ballistic Perforation Dynamics," *J. Appl. Mech.*, Vol. 30, Series E, No. 3 (September 1963).

An iterative procedure determines, by trial and correction, the empirical constants a and b that give the best agreement between calculations done at a predetermined number of impact speeds and the predictions of the above empirical formula.

For a given system, data on residual speed as a function of impact speed for impacts at normal incidence is fit to Equation 40 by a least-squares fit of the data to the linear expression

$$Y = MX + B \tag{41}$$

where $Y = V_x^2$, $X = V_s^2$, $M = R^2$, and $B = R^2V_o^2$. Trial values of a and b are then selected and used in the analytical model for impacts at normal incidence to obtain predictions of residual speeds that are compared with the empirical equation. An iterative procedure then introduces small changes in a and b systematically, so that differences between the predicted results and experimental results are minimized.

The trial values are

$$a = mV_o^2/2\pi R_s^2 \tag{42}$$

$$b = mR^2/2\pi R_s^2 \tag{43}$$

These values are used in the analytical procedure for normal incidence to determine the residual speed for several impact speeds. These pairs of residual speeds and impact speeds are then used to determine a pair of values of R and V_o by the same curve-fitting procedure that was used on the empirical data. Constant a is varied by a predetermined value, da, and another pair of values for R and V_o is calculated. Then b is varied by a predetermined amount, db, and a new pair of values of R and V_o is calculated. From the information available at this point, four partial derivatives are approximated by finite differences as

$$\frac{\partial V_o}{\partial a} = \frac{V_o\ (a + da,b) - V_o\ (a,b)}{da} \tag{44}$$

$$\frac{\partial R}{\partial a} = \frac{R(a + da,b) - R(a,b)}{da} \tag{45}$$

$$\frac{\partial V_o}{\partial b} = \frac{V_o\ (a,b + db) - V_o\ (a,b)}{db} \tag{46}$$

$$\frac{\partial R}{\partial b} = \frac{R(a,b + db) - R(a,b)}{db} \tag{47}$$

These partial derivatives and the differences $dV_o = V_o$ (experimental) $- V_o$ (a,b) and $dR = R$ (experimental) $- R$ (a,b) are used to determine new values of da and db by solving the equations

$$dV_o = \frac{\partial V_o}{\partial a} da + \frac{\partial V_o}{\partial b} db \tag{48}$$

and

$$dR = \frac{\partial R}{\partial a} da + \frac{\partial R}{\partial b} db \tag{49}$$

and the process is repeated until the differences are below some preset value.

In summary, this model of impact dynamics requires basic parameters that define the configuration, size, and inertia of the system. In addition, this model uses four empirical constants that define the material response of the plate to impact. Two empirical constants, P^* and α^*, are determined from observations on the depth of penetration required for the failure of the plate and on location of the failure. The other two constants, a and b, are determined by a best fit to data on the residual speed as a function of impact speed for normal incidence. Calculations of residual speeds, exit obliquities, and trajectories of the sphere through the plates are compared directly with experimental data. The degree of agreement is taken as a measure of success in modeling the dynamics of the impact. The agreement is very good at normal incidence where it is essentially a fit to that data, and agreement merely shows that it is possible to fit experimental data by means of the given procedure. The degree of agreement at other obliquities indicates success in extending the model of impact dynamics to the more complicated conditions of oblique impact.

COMPARISON OF ANALYTICAL PREDICTIONS AND EXPERIMENTAL DATA

The experimental part of this work consisted of experimental firings of spheres against steel and aluminum alloy plates. The firings were covered by high-speed photographic instrumentation, electronic measurement of impact speed, and measurement of craters produced in the target plates. The final form of the data is the correlation of the exit speed and obliquity of the sphere with its initial speed and obliquity, and measurement of the craters that were formed at particular impact speeds and obliquities.

Chosen for this experimental work were 6.35-mm spheres of SAE 52100 alloy steel. The target plates were 6061-T6 and 2024-T3 aluminum alloy, and a mild steel plate (SAE 1010). The aluminum alloy plates varied from 1.27 to 9.53 mm in thickness. The steel plates were all 1.47 mm thick. Firings were performed with the plates at normal incidence to the path of the projectile in order to collect sufficient data to determine the constants needed for the expression for the force on the sphere. Table 1 lists the values of a, b, P^*, and α^* that were determined from the data at normal incidence. Additional firings at oblique incidence were performed at 30, 45, and 60 degrees as a rule, but a few data were collected for 20, 50, and 70 degrees.

TABLE 1. Constants Determined From Data at Normal Incidence.

Target plate material	Target plate thickness, mm	Constants			
		P^*, mm	α^*, deg	a, N/m^2	b, kg/m^3
2024-T3 aluminum alloy.....	1.27	2.2	45	0.272×10^9	0.129×10^4
	3.18	3.0	45	0.101×10^{10}	0.126×10^4
	6.35	6.4	45	0.933×10^9	0.974×10^3
	9.52	7.5	45	0.112×10^{10}	0.580×10^3
SAE 1010 steel...	1.47	4.6	45	0.380×10^9	0.148×10^4

A given sphere and plate constitute a system. Correlation of the final state of motion of the sphere to the initial state of motion is a measure of the impact behavior of the system. The accuracy of the prediction of this correlation is taken as an index of the accuracy of modeling of the system during impact. Impact systems of the same material but different plate thicknesses constitute a family of systems. The case of the steel sphere and aluminum plates has been investigated as a family, and it is possible to come to conclusions about the family, especially as to the meaning of the constants for the force expression as a function of plate thickness.

STEEL SPHERES IMPACTING AGAINST ALUMINUM PLATES

Figure 11 shows experimental data compared to the analytical representation for firings of 6.35-mm steel spheres against 9.53-mm aluminum plates at normal incidence. The data points are the results of experimental firings. The line represents the analytical predictions based on the model described above and the values of constants a and b in the expression for the contact force that give the best fit to the data.

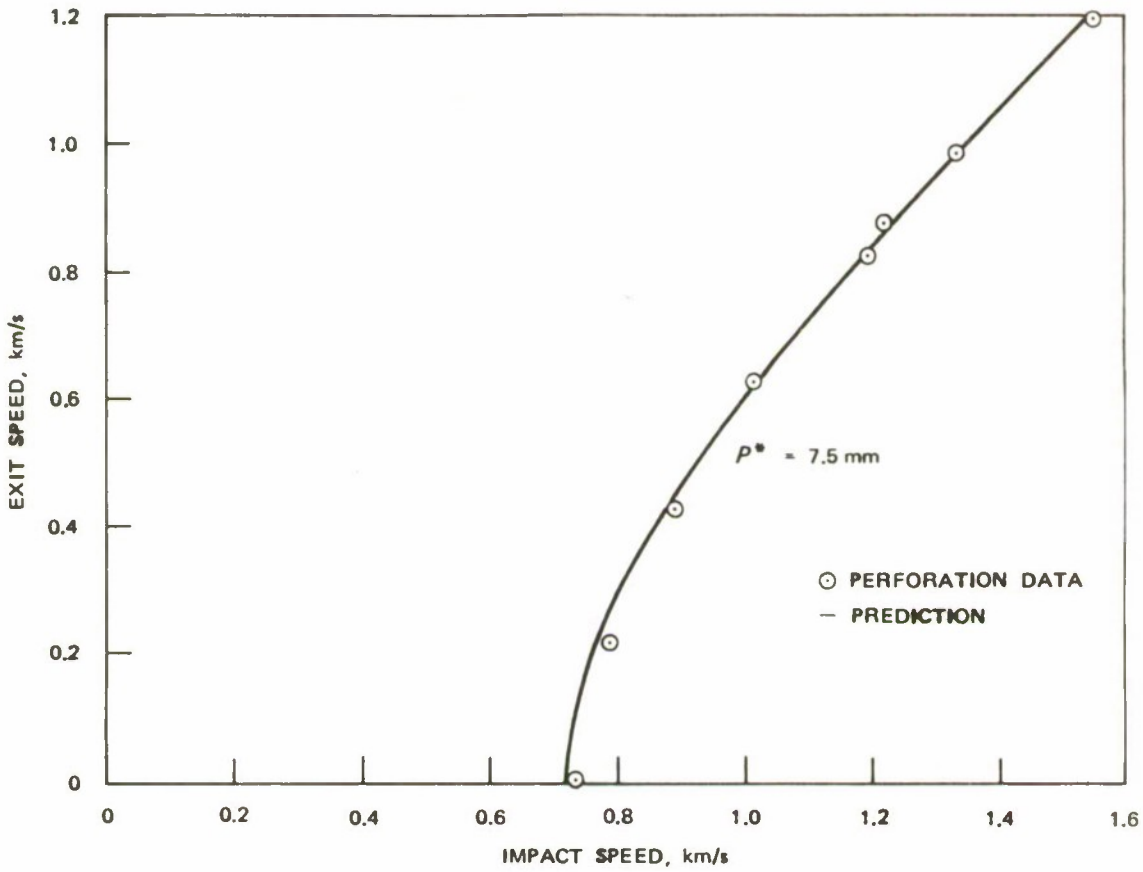

FIGURE 11. Data and Predictions of Exit Speeds for 6.35-mm Spheres Fired Against 6061 Aluminum Alloy Targets of 9.53-mm Thickness at Zero Degree Obliquity.

This comparison is only an indication of the consistency of the analytical procedure with the experimental data. It demonstrates the feasibility of finding constants for the empirical expression for the contact force in the analytical model, and results in predictions consistent with data used to derive the constants.

Agreement between predictions at obliquity and experimental data is considerably more significant than the agreement at normal incidence because there are qualitative features of the data predicted by the model that are not obvious from the data at normal incidence. The system with the largest plate thickness is chosen first because this system displays these qualitative features in a particularly simple form.

Thick-Plate Ricochet

Figures 12 through 17 show a comparison of experimental data and analytical predictions for firings of 6.35-mm spheres against 6061-T6 aluminum alloy targets at 20, 45, and 60 degrees obliquity. For each obliquity there is a range of impact speeds in which the sphere ricochets, a range in which it embeds, and a range in which it perforates (see Figure 12). There is reasonable agreement between the experimental data and the predictions as to the extent of these ranges. The curves of residual speed in the ricochet range are roughly sinusoidal. The corresponding ricochet obliquities increase monotonically from a value above 90 to 180 degrees and then remain constant. This is what the model predicts, and the experimental data in general agree with these predictions. In the embedment range the residual speed is zero, but the analytical predictions assign an obliquity to every impact speed in the embedment range. The obliquity assigned is the last obliquity angle the projectile has as it comes to rest. In terms of the trajectory of the sphere, it is the terminal direction of the trajectory. Examples of these predictions are shown in the embedment zones of Figures 13, 15, and 17. In the perforation range the residual speed curves are of gradually decreasing curvature, and the corresponding curves for the obliquity after perforation rise rapidly and approach the incident obliquity.

Figures 18 through 24 illustrate the same kind of comparison of predictions and data for a system consisting of a 6.35-mm sphere and 2024-T3 aluminum alloy plates of 6.35-mm thickness. The boundaries of the embedment, ricochet, and perforation ranges are changed, but the qualitative descriptions of the correlations in each range remain the same. The system with the 9.53-mm 6061-T6 aluminum alloy plates and the system with the 6.35-mm 2024-T3 aluminum alloy plates both have the important characteristic that the plate fails at deep penetrations.

Consider the trajectories of a projectile in the ricochet and embedment range. As impact speed increases, the maximum penetration increases. This is predicted by the model and observed in experimental firings. If the plate is sufficiently thick, the sphere will never achieve the penetration required for the failure of the plate on a trajectory that is of the ricochet type. Instead, failure will occur on a trajectory that ends in embedment even though the plate has failed at some point along the trajectory.

These two systems exhibit what may be called "thick-plate ricochet behavior." The correlation of exit speed with impact speed is smooth and symmetrical. The correlation of exit obliquity with impact speed is a smooth increase to a flat top. These are the characteristics of ricochet with no tear or fracture failures that go completely through the plate.

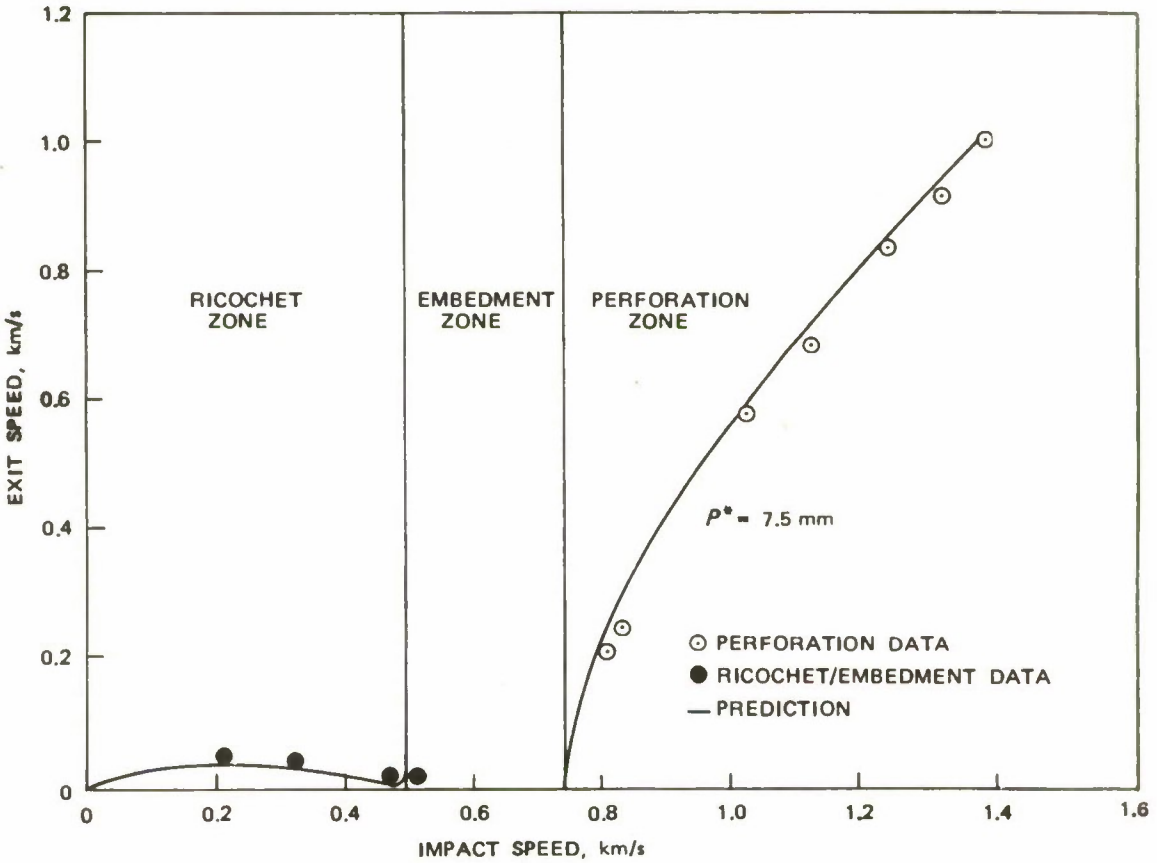

FIGURE 12. Data and Predictions of Exit Speeds for 6.35-mm Spheres Fired Against 6061 Aluminum Alloy Targets of 9.53-mm Thickness at 20 Degrees Obliquity.

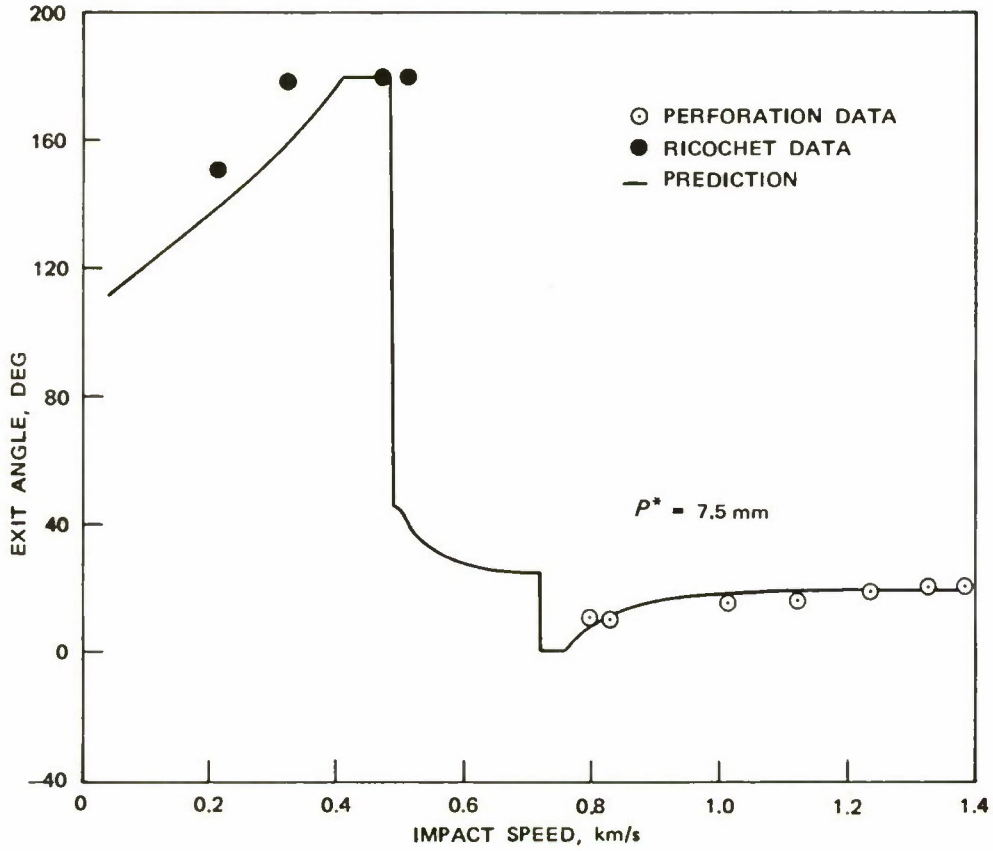

FIGURE 13. Data and Predictions of Exit Obliquities for 6.35-mm Spheres Fired Against 6061 Aluminum Alloy Targets of 9.53-mm Thickness at 20 Degrees Obliquity.

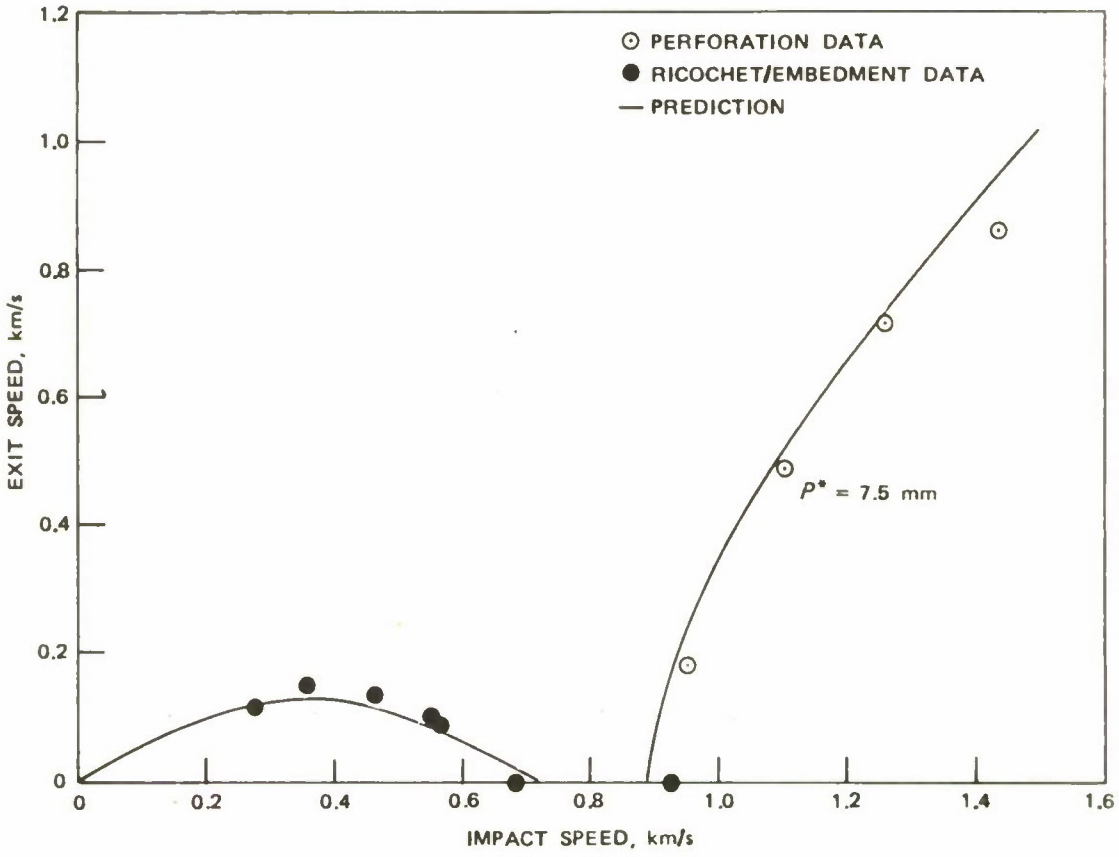

FIGURE 14. Data and Predictions of Exit Speeds for 6.35-mm Spheres Fired Against 6061 Aluminum Alloy Targets of 9.53-mm Thickness at 45 Degrees Obliquity.

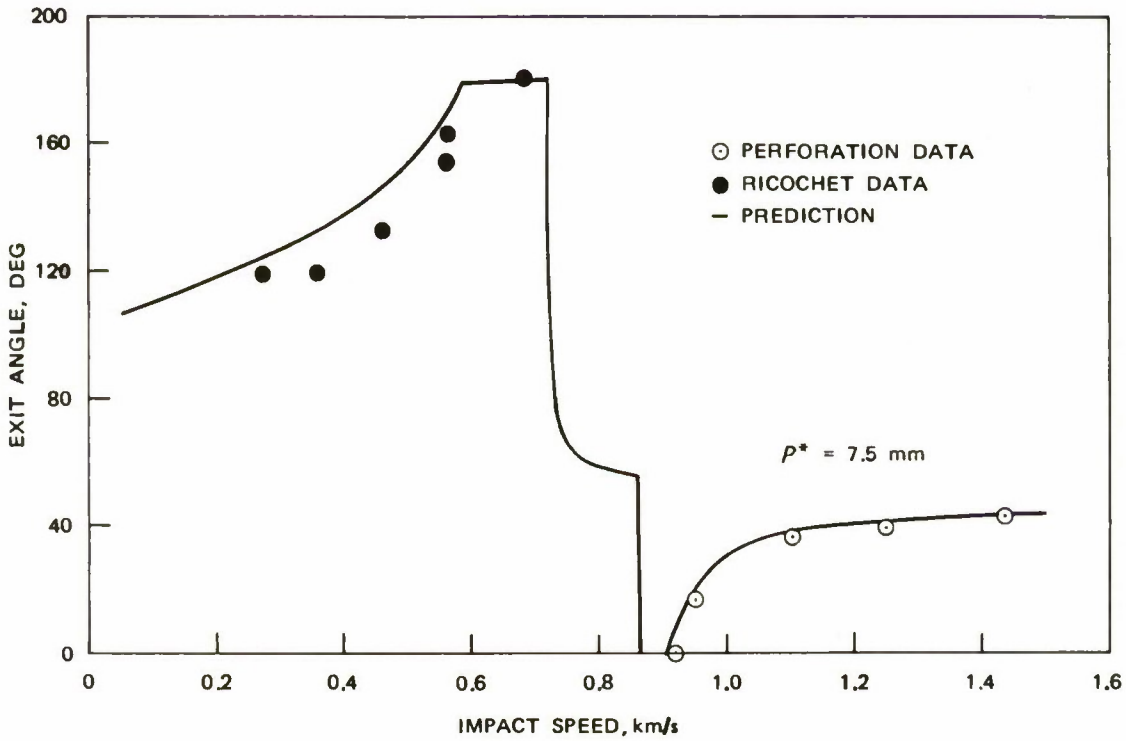

FIGURE 15. Data and Predictions of Exit Obliquities for 6.35-mm Spheres Fired Against 6061 Aluminum Alloy Targets of 9.53-mm Thickness at 45 Degrees Obliquity.

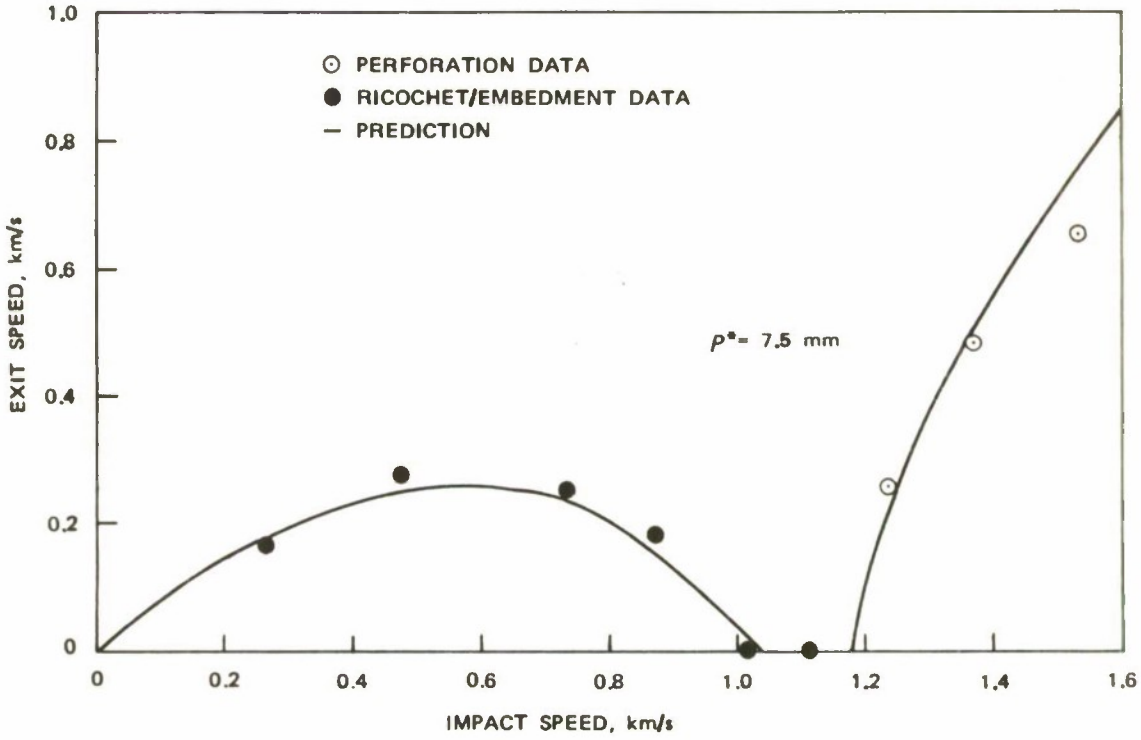

FIGURE 16. Data and Predictions of Exit Speeds for 6.35-mm Spheres Fired Against 6061 Aluminum Alloy Targets of 9.53-mm Thickness at 60 Degrees Obliquity.

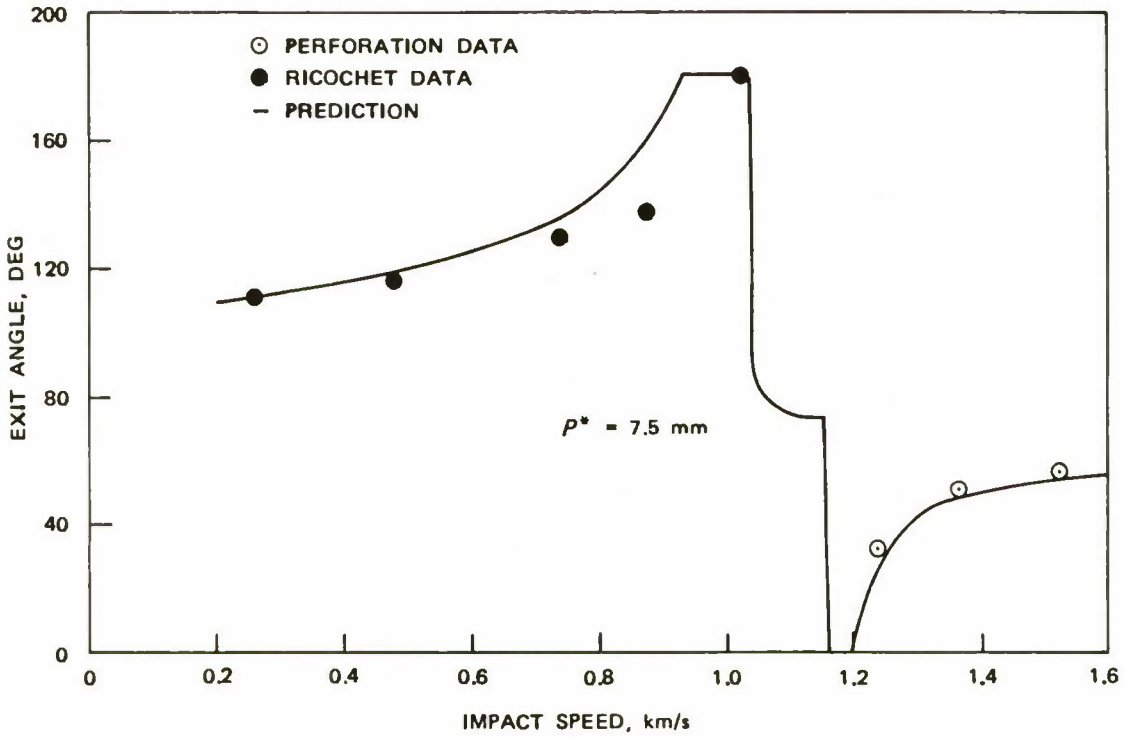

FIGURE 17. Data and Predictions of Exit Obliquities for 6.35-mm Spheres Fired Against 6061 Aluminum Alloy Targets of 9.53-mm Thickness at 60 Degrees Obliquity.

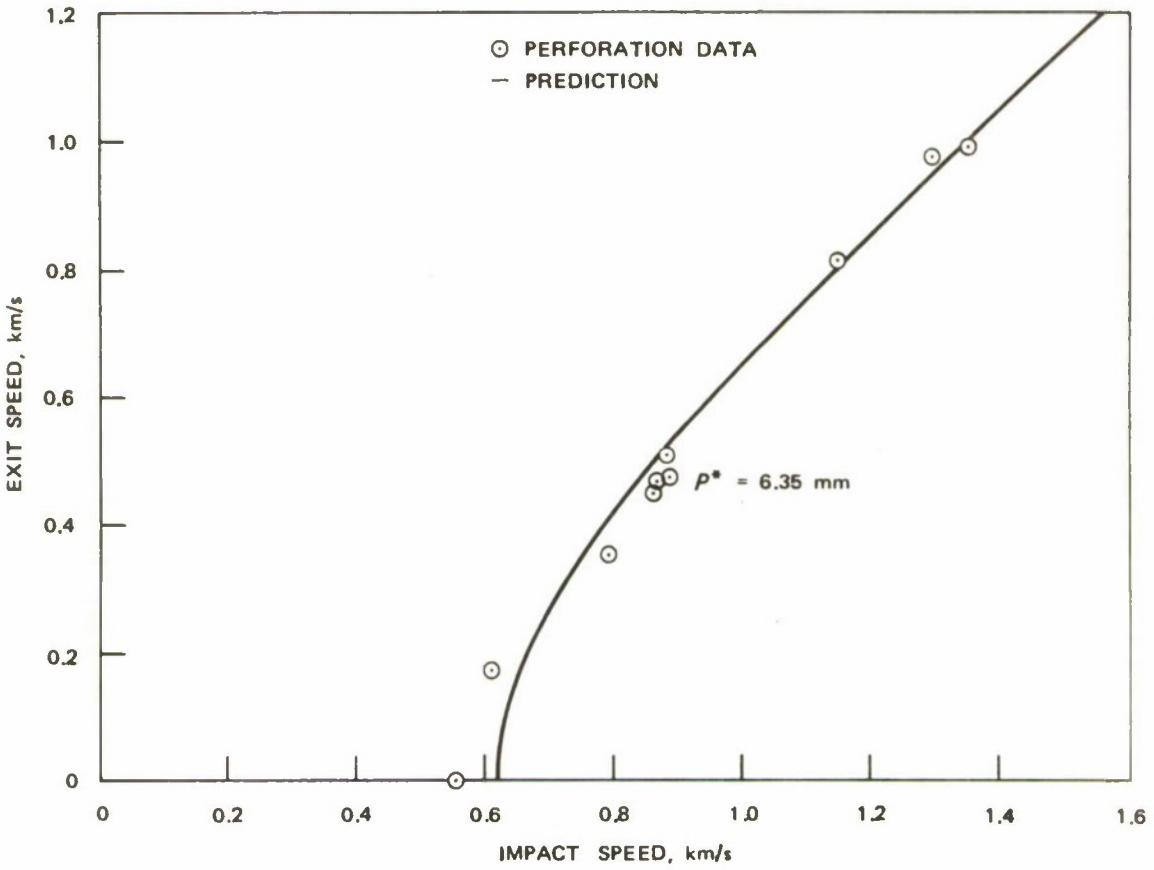

FIGURE 18. Data and Predictions of Exit Speeds for 6.35-mm Spheres Fired Against 2024 Aluminum Alloy Targets of 6.35-mm Thickness at Zero Degree Obliquity.

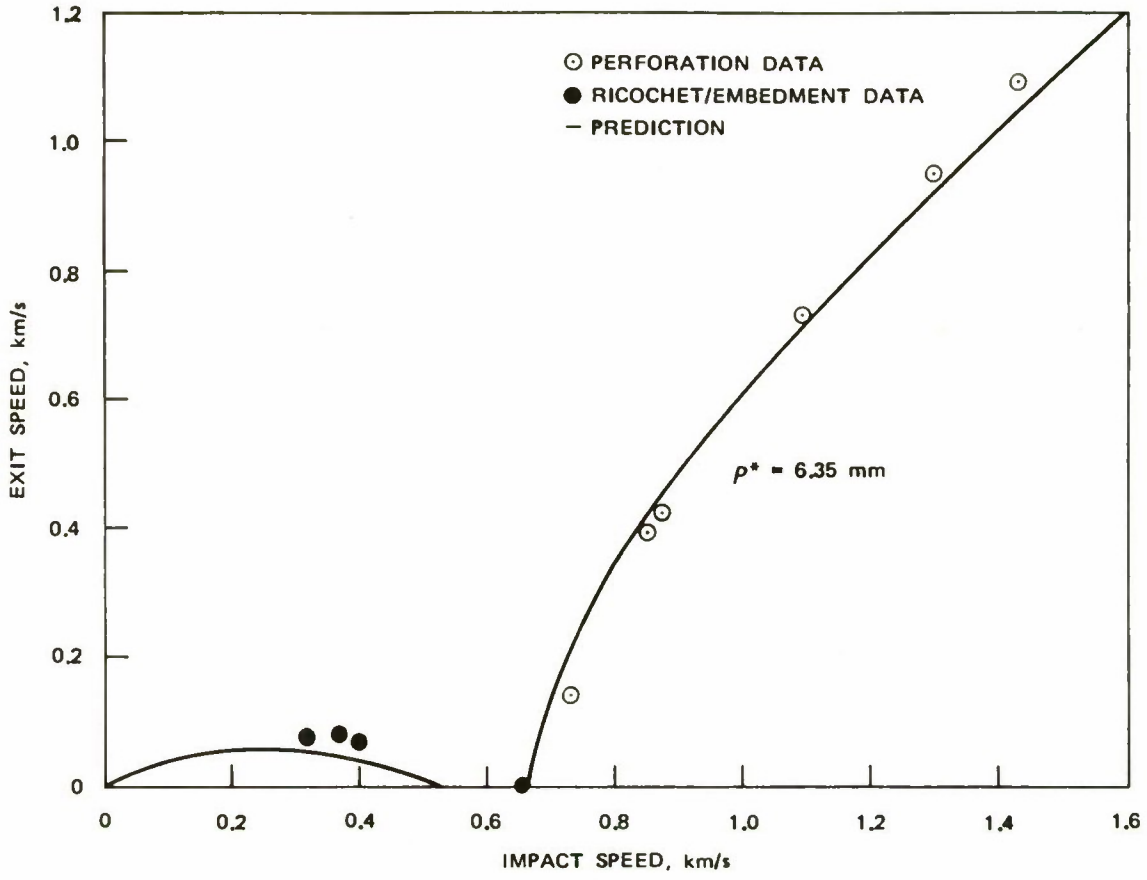

FIGURE 19. Data and Predictions of Exit Speeds for 6.35-mm Spheres Fired Against 2024 Aluminum Alloy Targets of 6.35-mm Thickness at 30 Degrees Obliquity.

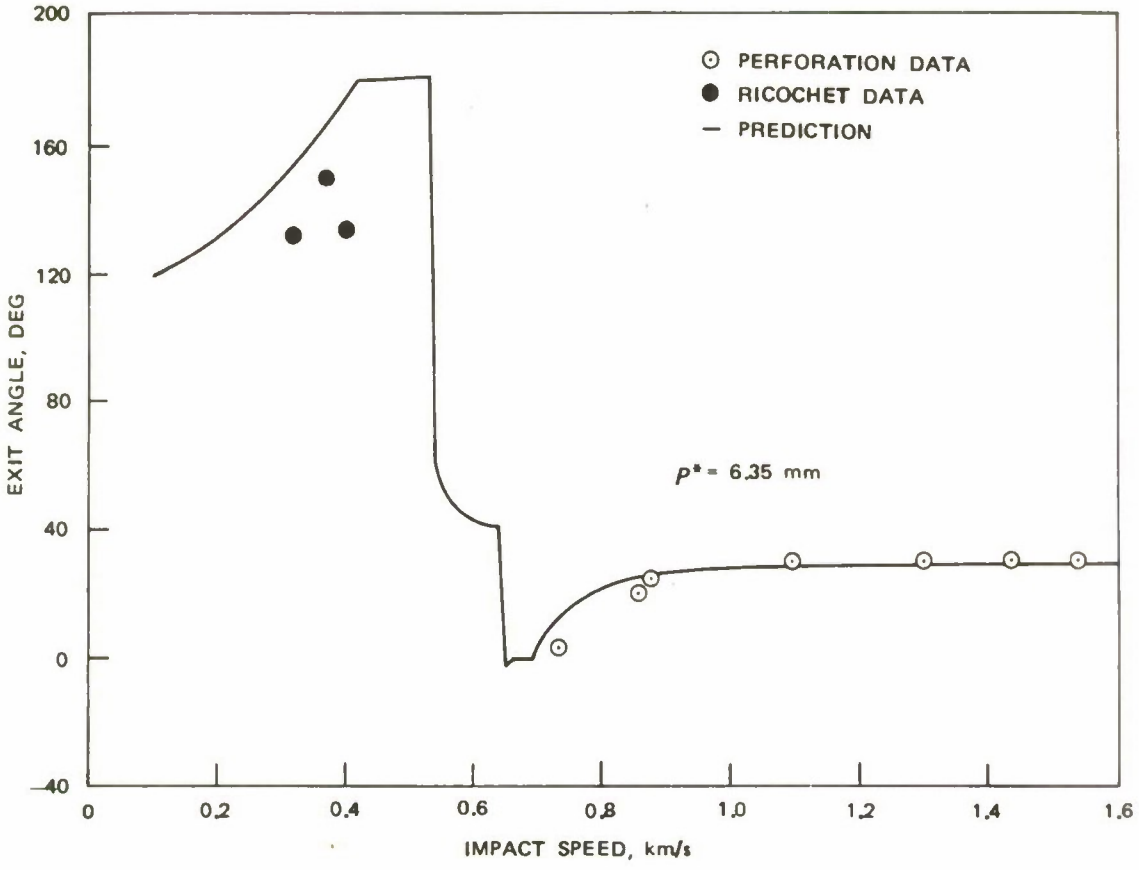

FIGURE 20. Data and Predictions of Exit Obliquities for 6.35-mm Spheres Fired Against 2024 Aluminum Alloy Targets of 6.35-mm Thickness at 30 Degrees Obliquity.

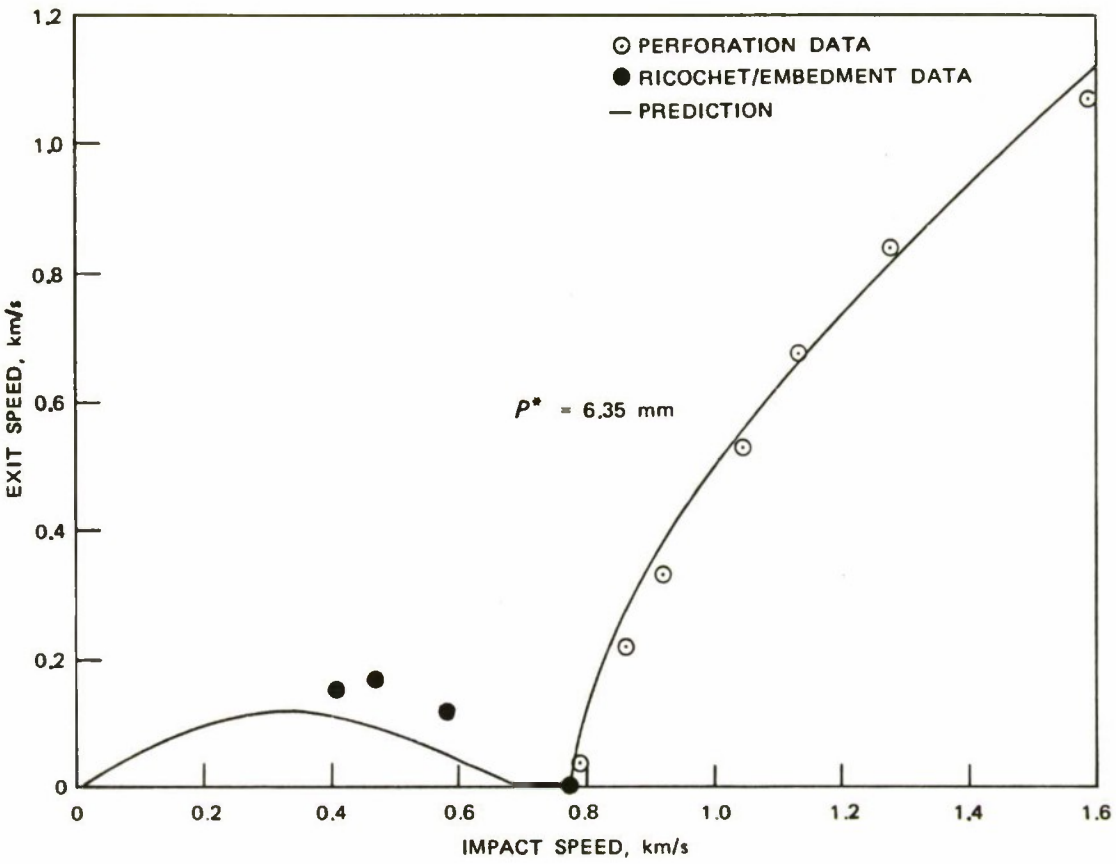

FIGURE 21. Data and Predictions of Exit Speeds for 6.35-mm Spheres Fired Against 2024 Aluminum Alloy Targets of 6.35-mm Thickness at 45 Degrees Obliquity.

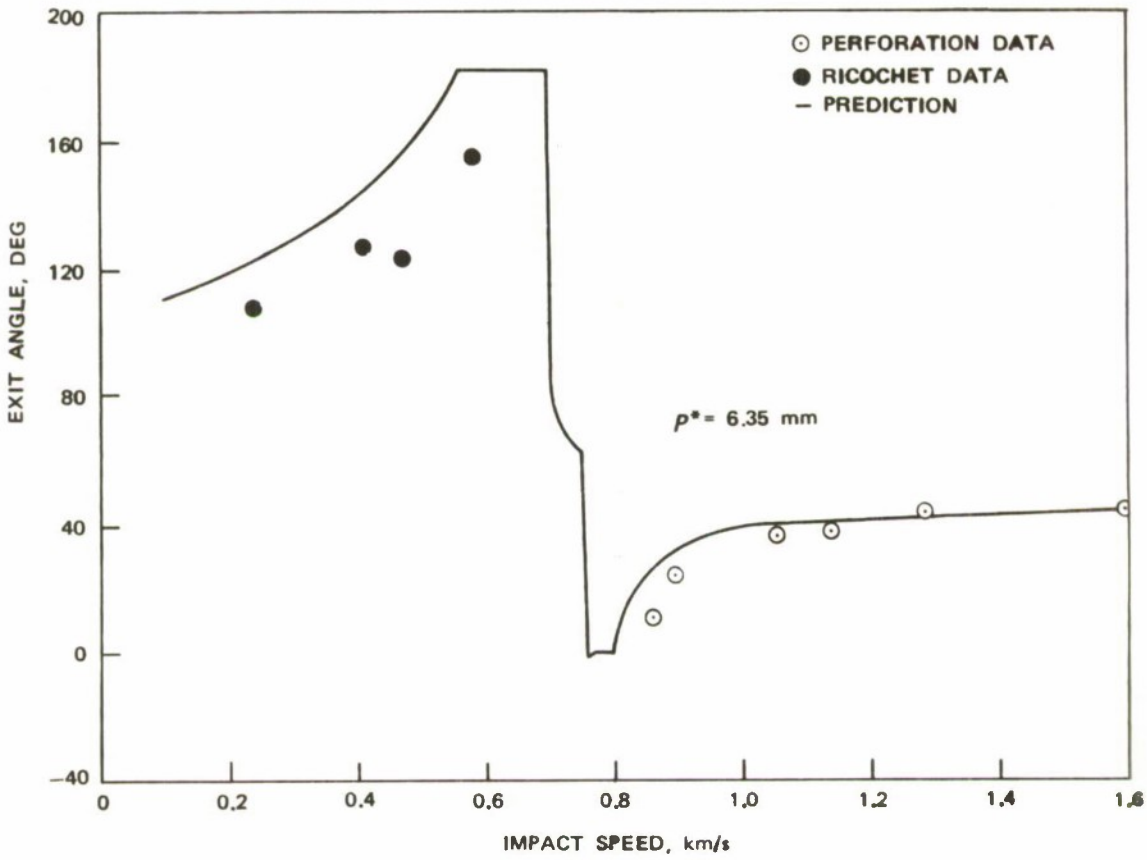

FIGURE 22. Data and Predictions of Exit Obliquities for 6.35-mm Spheres Fired Against 2024 Aluminum Alloy Targets of 6.35-mm Thickness at 45 Degrees Obliquity.

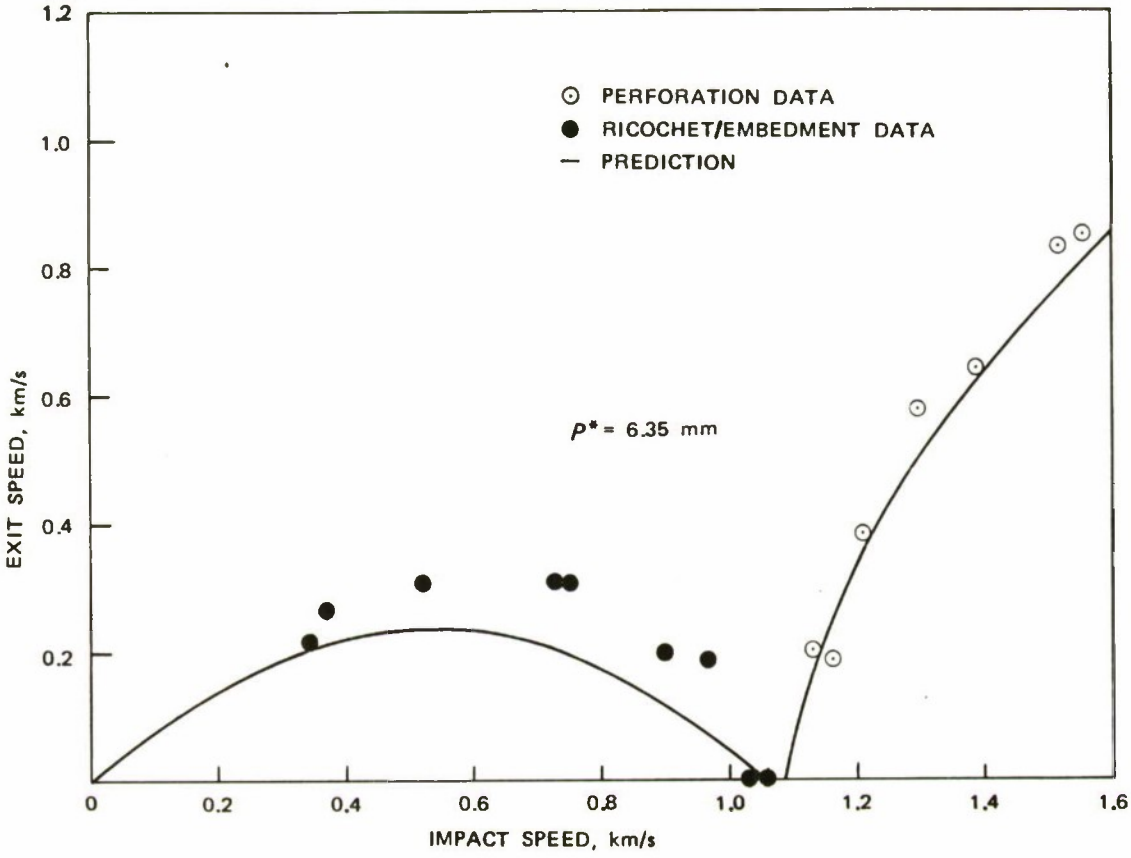

FIGURE 23. Data and Predictions of Exit Speeds for 6.35-mm Spheres Fired Against 2024 Aluminum Alloy Targets of 6.35-mm Thickness at 60 Degrees Obliquity.

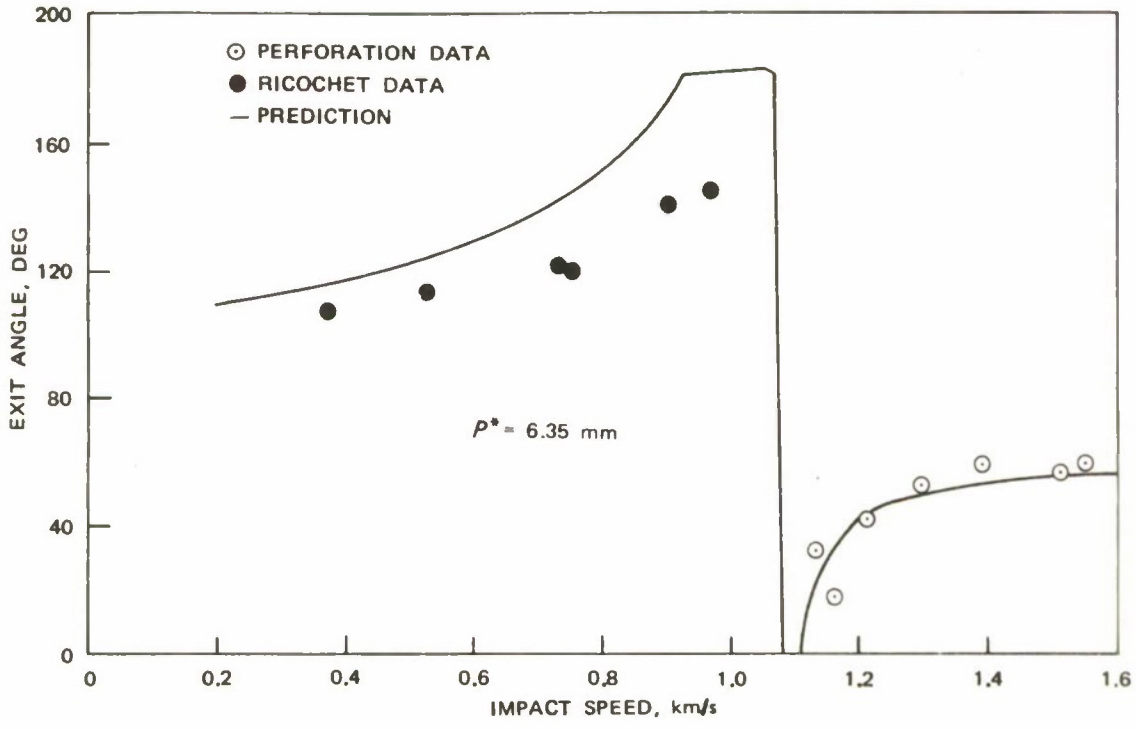

FIGURE 24. Data and Predictions of Exit Obliquities for 6.35-mm Spheres Fired Against 2024 Aluminum Alloy Targets of 6.35-mm Thickness at 60 Degrees Obliquity.

Thin-Plate Ricochet

Figures 25 through 34 show behavior of a system consisting of a 6.35-mm sphere and either a 3.18- or a 1.27-mm 2024-T3 aluminum alloy plate. These correlations are similar to those for the thicker plates. The most conspicuous differences are that correlations of exit speed with impact speed are not symmetrically shaped, and correlations of exit obliquity with impact speed have pronounced spikes near the embedment range. These differences are caused by ultimate failure of the plate in the ricochet range. Failure occurs along a trajectory that ends in ricochet without failure. Failure influences the trajectory, but not enough to result in either embedment or perforation. The effect is rather to ricochet, but at a lower exit speed and a higher exit obliquity. There is a small range of impact speeds for which this modified form of ricochet occurs. For speeds above this range the trajectories end in embedment.

In a given family of impact systems, this change in behavior is correlated with thickness, and below some critical thickness the systems of

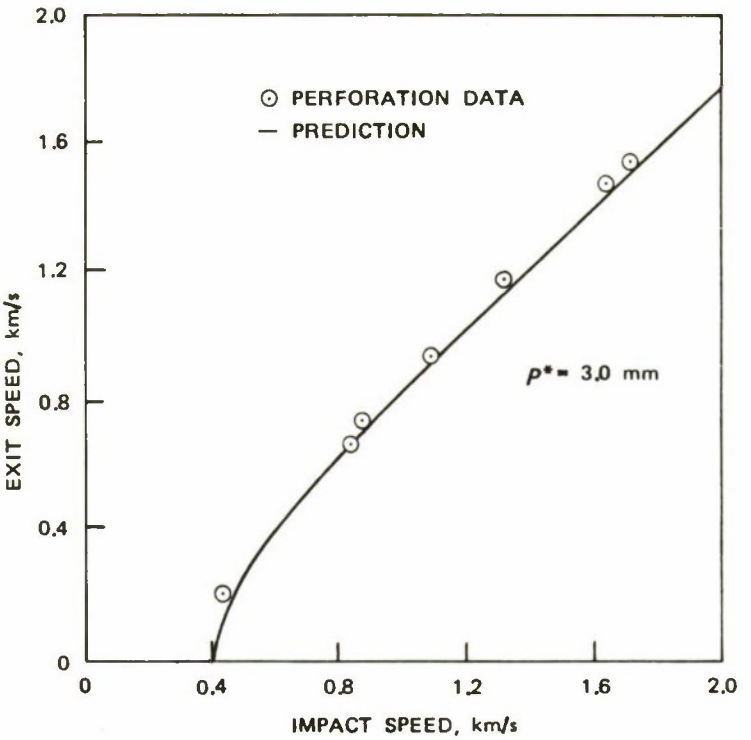

FIGURE 25. Data and Predictions of Exit Speeds for 6.35-mm Spheres Fired Against 2024 Aluminum Alloy Targets of 3.18-mm Thickness at Zero Degree Obliquity.

a family will always show this kind of behavior. The controlling physical phenomena are the processes of failure in the plate that take place at lower velocities as the plate thickness is decreased. The dashed lines in Figures 30 and 31 are analytical predictions using an extremely large value of the critical penetration. This shows the thick-plate behavior of the system compared with the actual thin-plate behavior of the system.

The comparison between experimental data and analytical prediction leads to the conclusion that the analytical model is sufficiently accurate to fit data at normal incidence by means of its empirical constants. In addition, it can predict qualitative features of the results of impact at oblique incidence that are not evident from observations at normal incidence. Such features as the spikes in the correlations of exit obliquities with impact speed and the rapid drops in the correlations of exit speed with impact speed are unforeseen consequences of the model of impact dynamics. The existence of these features is predicted and found to be in reasonable quantitative agreement with experimental observations.

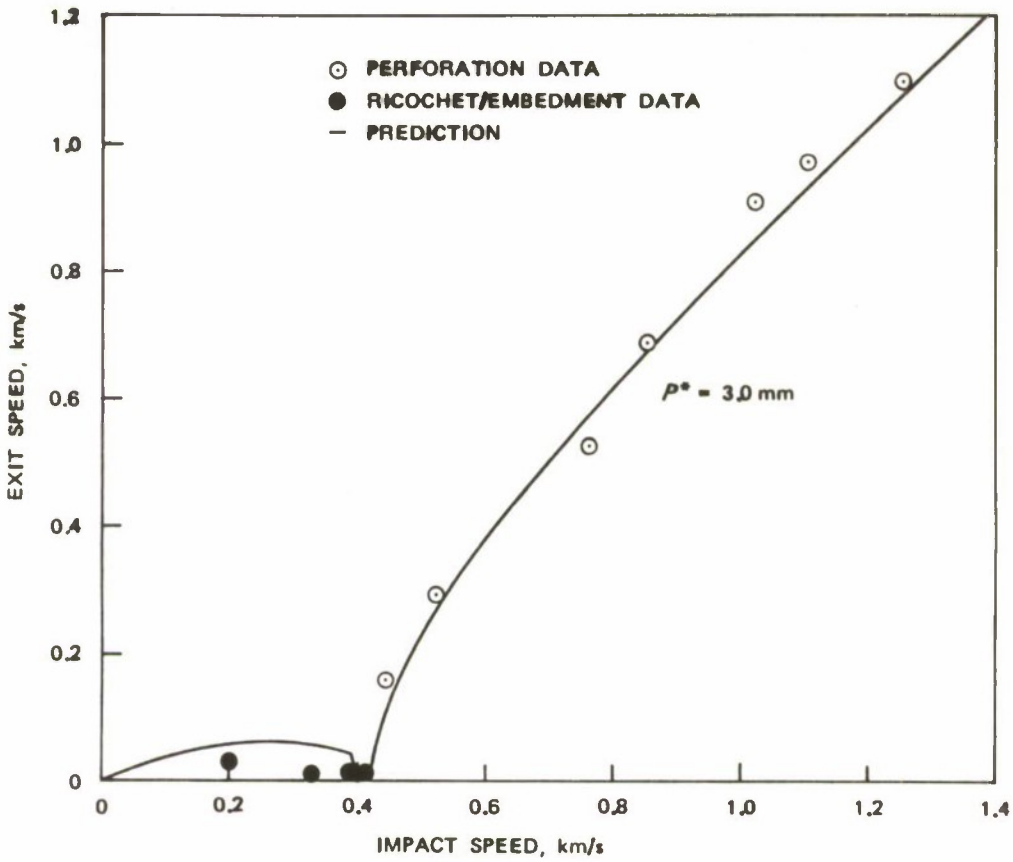

FIGURE 26. Data and Predictions of Exit Speeds for 6.35-mm Spheres Fired Against 2024 Aluminum Alloy Targets of 3.18-mm Thickness at 30 Degrees Obliquity.

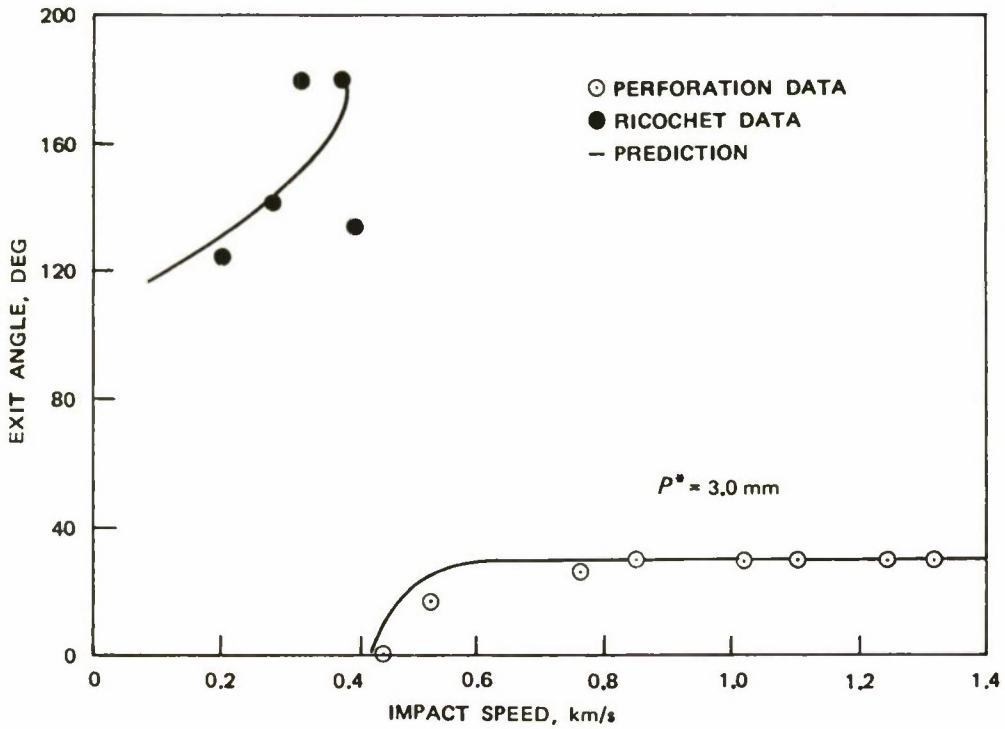

FIGURE 27. Data and Predictions of Exit Obliquities for 6.35-mm Spheres Fired Against 2024 Aluminum Alloy Targets of 3.18-mm Thickness at 30 Degrees Obliquity.

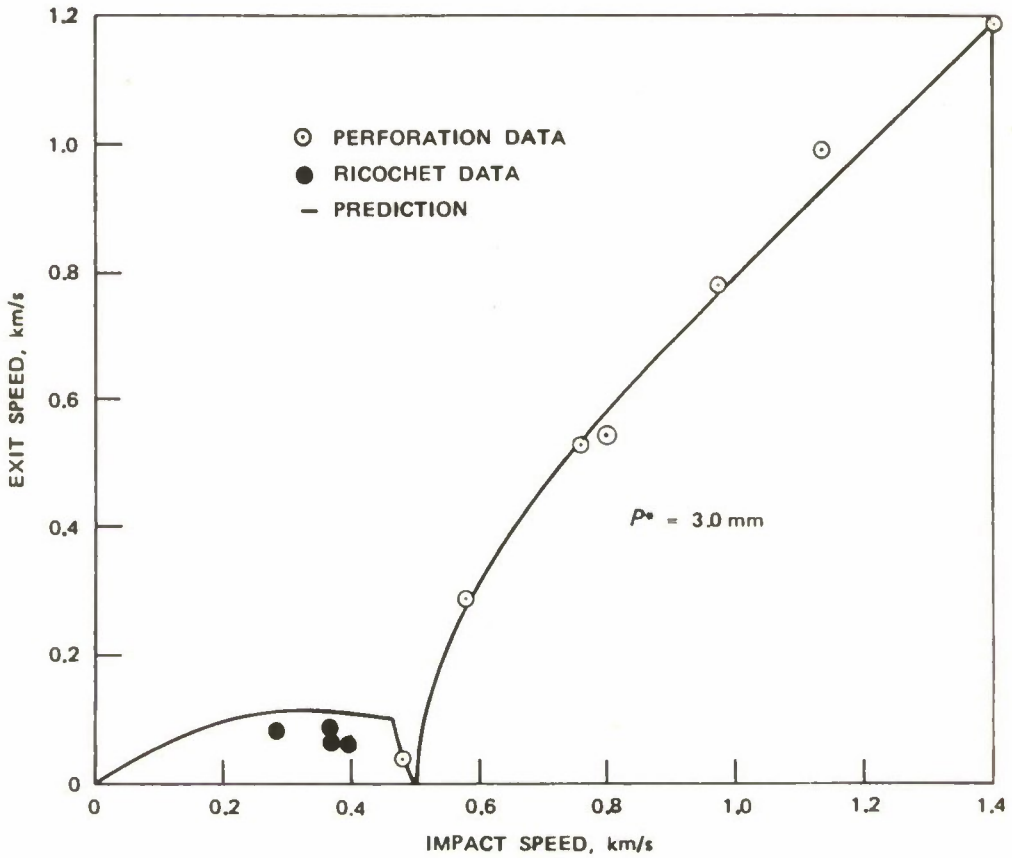

FIGURE 28. Data and Predictions of Exit Speeds for 6.35-mm Spheres Fired Against 2024 Aluminum Alloy Targets of 3.18-mm Thickness at 45 Degrees Obliquity.

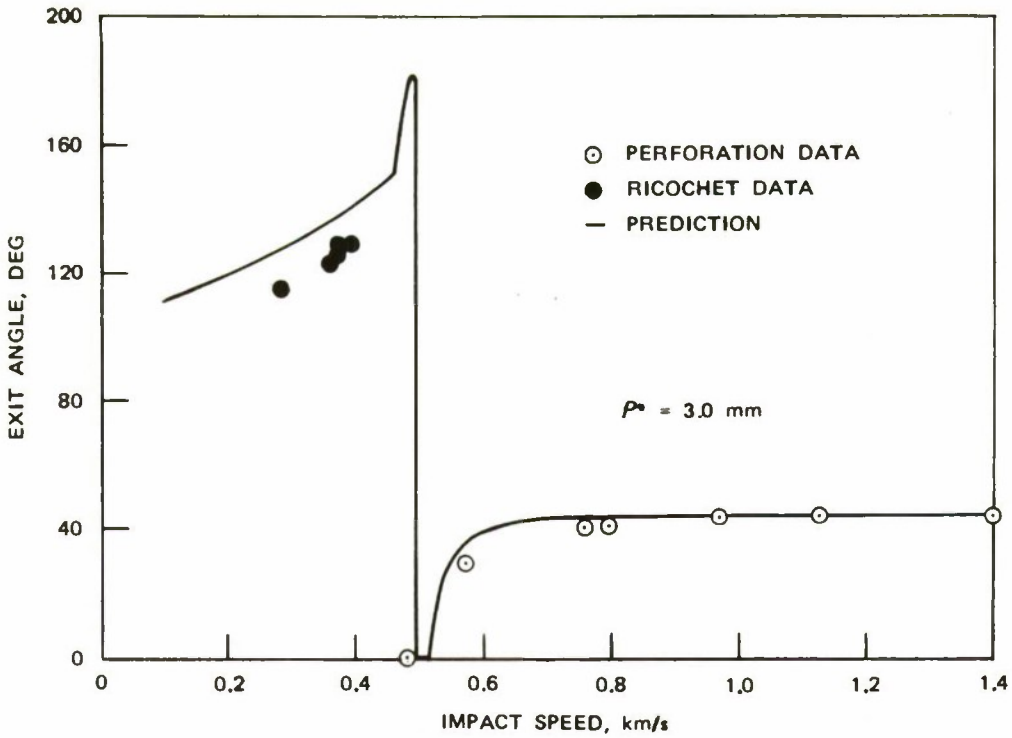

FIGURE 29. Data and Predictions of Exit Obliquities for 6.35-mm Spheres Fired Against 2024 Aluminum Alloy Targets of 3.18-mm Thickness at 45 Degrees Obliquity.

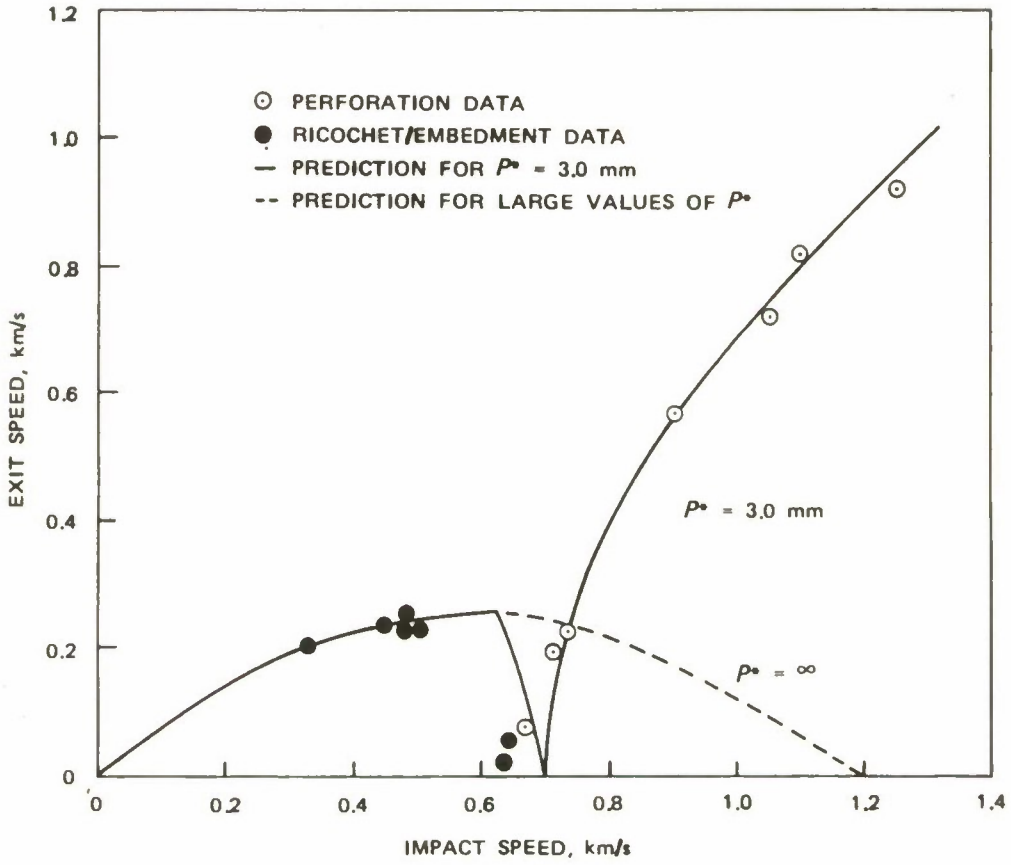

FIGURE 30. Data and Predictions of Exit Speeds for 6.35-mm Spheres Fired Against 2024 Aluminum Alloy Targets of 3.18-mm Thickness at 60 Degrees Obliquity.

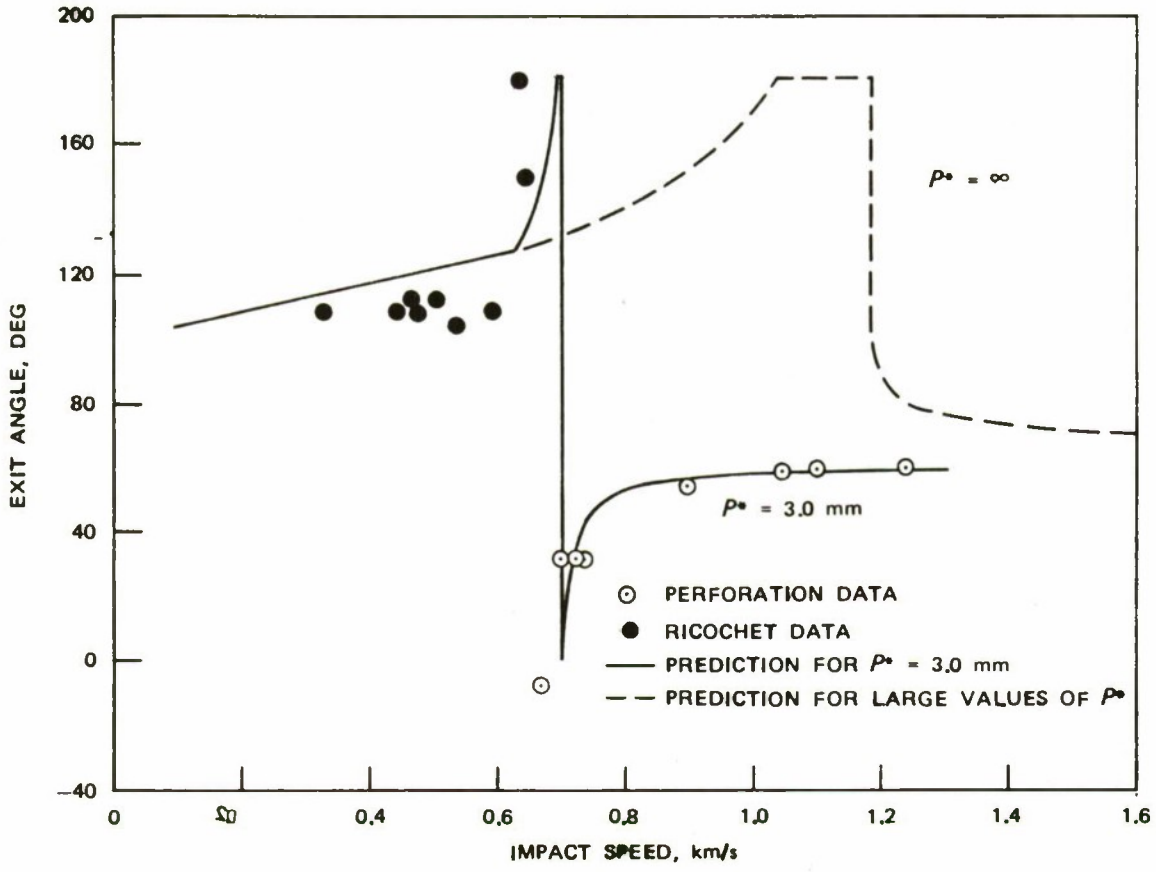

FIGURE 31. Data and Predictions of Exit Obliquities for 6.35-mm Spheres Fired Against 2024 Aluminum Alloy Targets of 3.18-mm Thickness at 60 Degrees Obliquity.

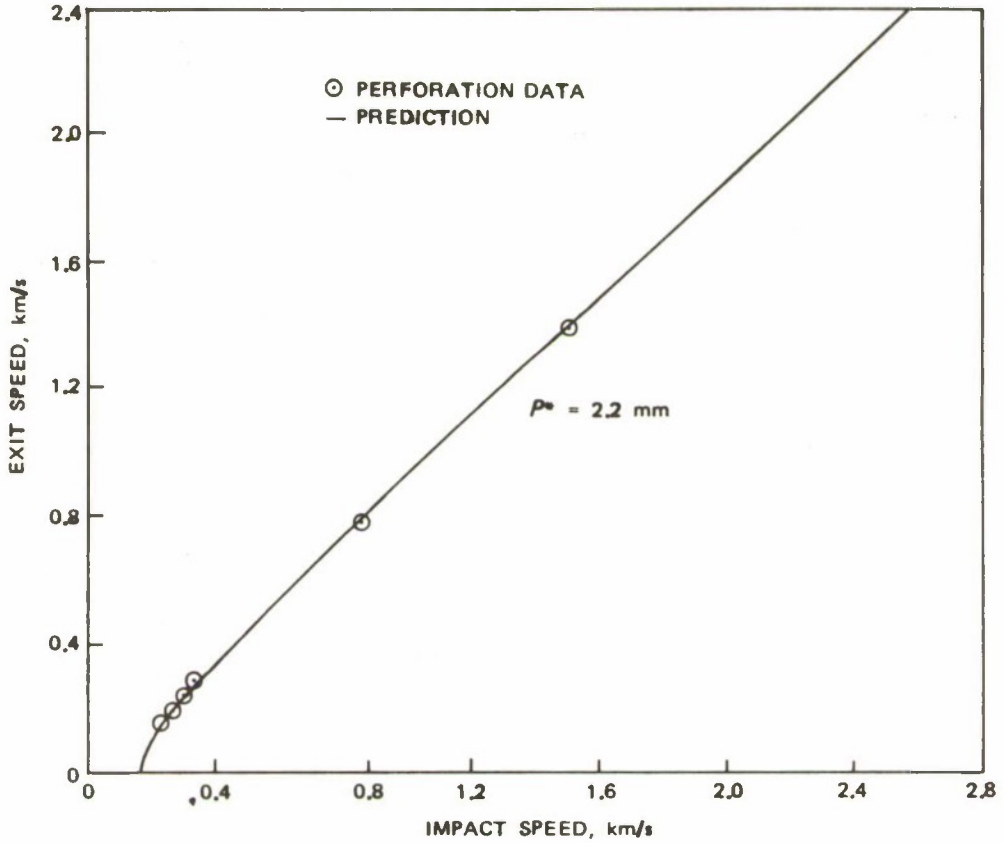

FIGURE 32. Data and Predictions of Exit Speeds for 6.35-mm Spheres Fired Against 2024 Aluminum Alloy Targets of 1.27-mm Thickness at Zero Degree Obliquity.

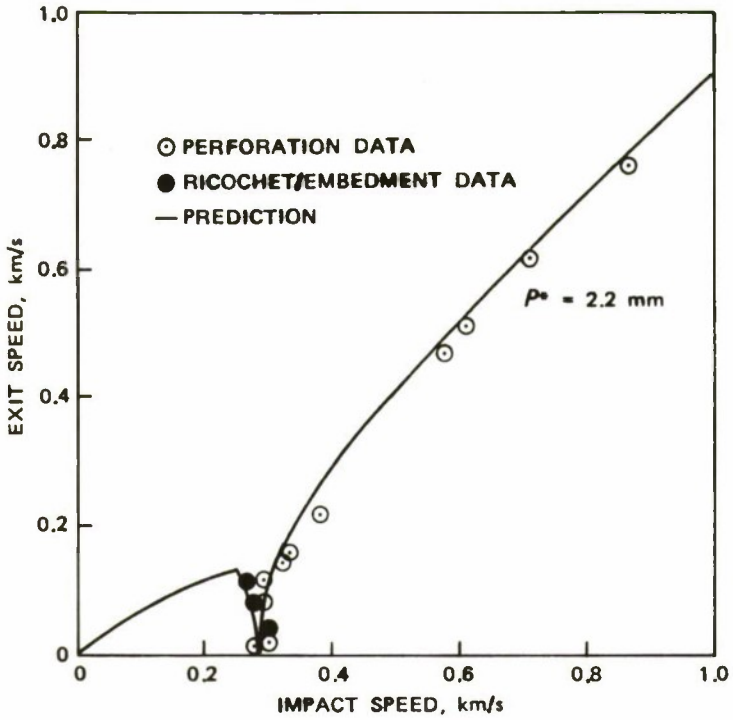

FIGURE 33. Data and Predictions of Exit Speeds for 6.35-mm Spheres Fired Against 2024 Aluminum Alloy Targets of 1.27-mm Thickness at 60 Degrees Obliquity.

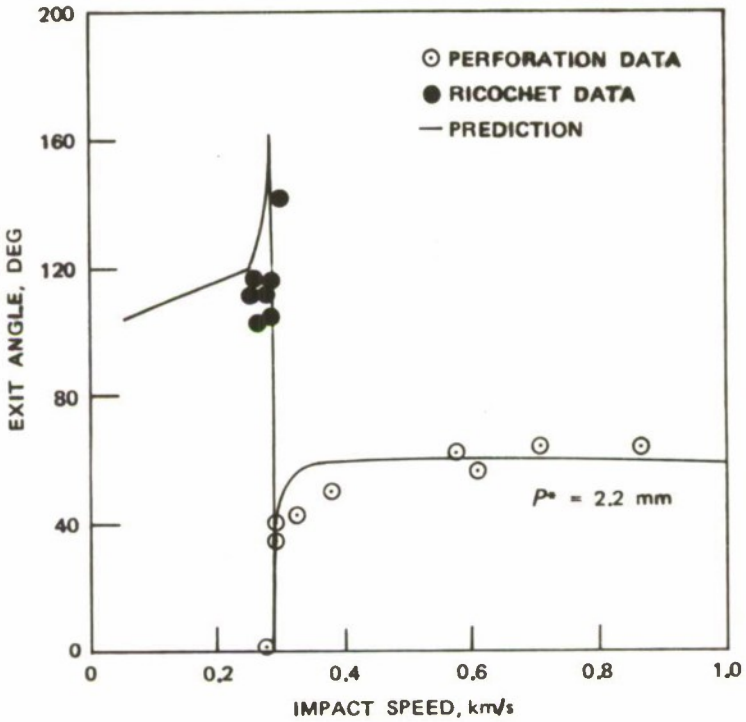

FIGURE 34. Data and Predictions of Exit Obliquities for 6.35-mm Spheres Fired Against 2024 Aluminum Alloy Targets of 1.27-mm Thickness at 60 Degrees Obliquity.

Crater-Shape Predictions

Correlations between initial and final states of motion are useful representations of system behavior, and the accuracy with which a model predicts these correlations is one measure of the accuracy of the model for that system. Prediction of crater shapes for given impact speeds is an even more sensitive measure of the accuracy of a model.

Figure 35 compares actual crater shapes with predictions from the analytical model. The solid lines represent tracings of craters taken from a plate that has been cut through the crater in the direction of travel of the sphere. Dashed lines represent predictions derived from the trajectory of the sphere by applying Equations 31, 32, 37, and 38. The impact system is a 6.35-mm sphere impacting a 9.53-mm aluminum alloy plate at 60 degrees obliquity. The craters correspond to points in the ricochet and embedment ranges of Figures 16 and 17, the correlation of initial with final states of motion for this impact system.

The predictions and tracings have roughly similar shapes, but a significant difference in major dimensions. Actual craters are shorter and shallower than the predicted craters in the lower part of the ricochet range. With increasing impact speed, but remaining in the ricochet range, the actual crater length exceeds the predicted crater length, and the actual crater shape is more curved toward the exit end. In the embedment range, actual and predicted shapes are in reasonable agreement. Perforation craters offer the least evidence of the dynamics of the impact process because large sections of the craters are torn away.

Figure 36 compares tracings of crater shapes with predictions for the system consisting of a 6.35-mm sphere and a 6.35-mm aluminum alloy plate. These comparisons have the same trends as for the 9.53-mm 6061-T6 plates, but the difference between predicted and observed crater shapes is greater. This is consistent with the observation that predictions of the final states of motion are poorer for this plate as well.

Figure 37 compares tracings of crater shapes with predictions for a system consisting of a 6.35-mm sphere and a 3.18-mm 2024-T3 aluminum alloy plate. Comparisons for this system are considerably closer than for the 6.35-mm plate and show the same trends—an overprediction at lower speeds, and improved agreement with increased impact speed.

Steel Spheres Impacting Against Mild Steel Plates

It is not practical to conduct a study with steel plates comparable to the study with aluminum plates. The difficulty is that the greater density and strength of steel results in breakup of the sphere at moderate plate thicknesses. A series of experiments has been conducted with 1.47-mm-thick mild steel, and these data have revealed still other complexities in the behavior of mild steel

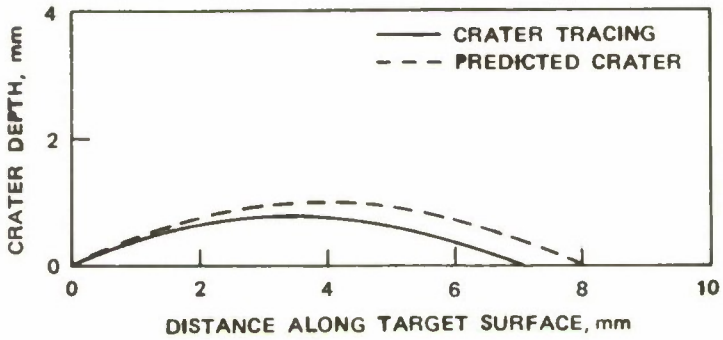

Impact speed, 0.263 km/s

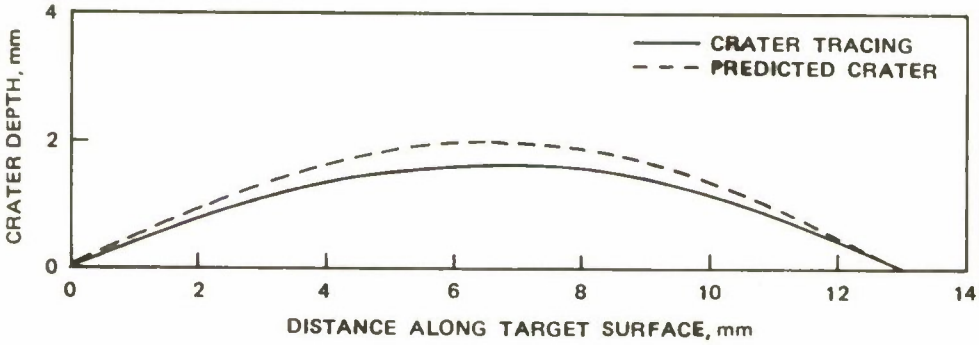

Impact speed, 0.475 km/s

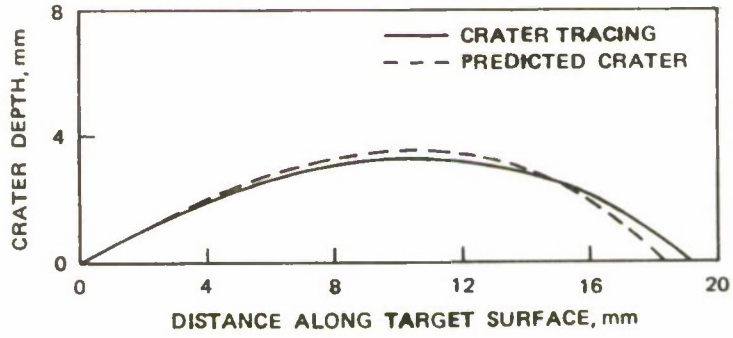

Impact speed, 0.737 km/s

FIGURE 35. Measured and Predicted Crater Shapes for the Impact of a 6.35-mm Sphere at 60 Degrees Obliquity Against a 6061 Aluminum Alloy Plate of 9.53-mm Thickness and at Various Impact Speeds.

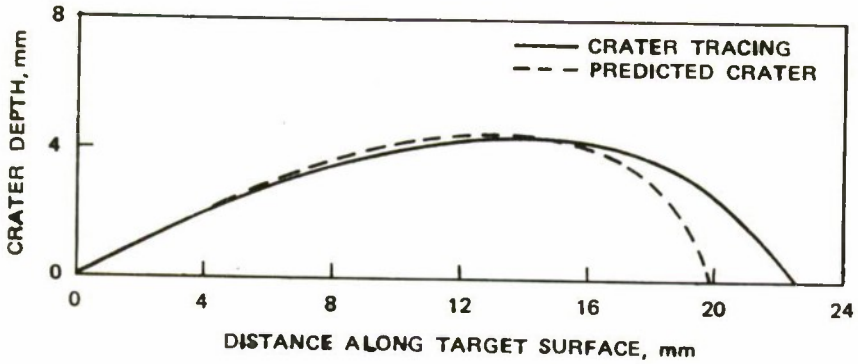

Impact speed, 0.869 km/s

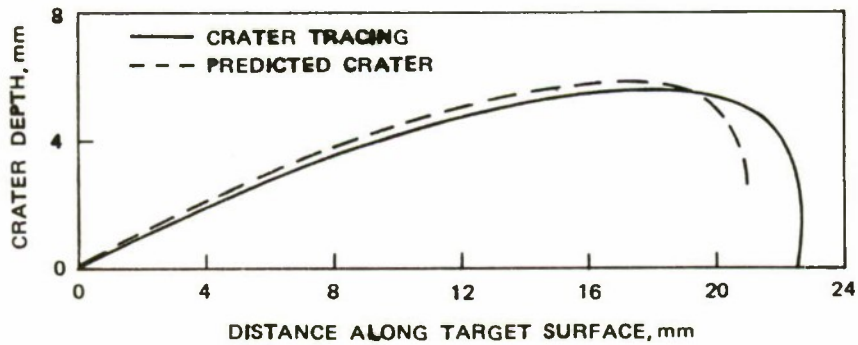

Impact speed, 1.021 km/s

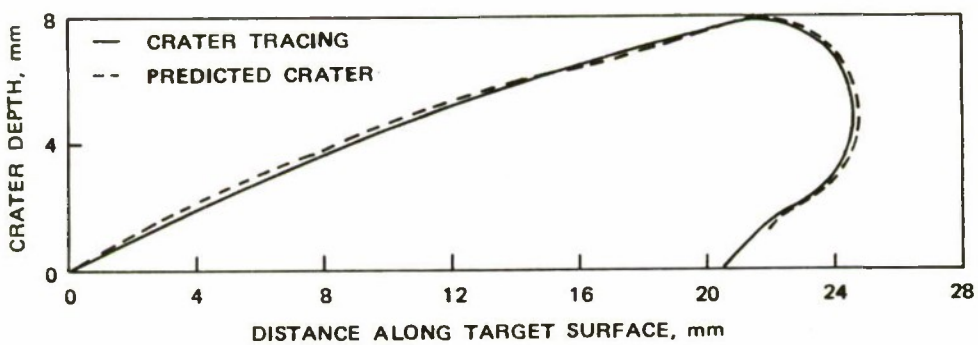

Impact speed, 1.112 km/s

FIGURE 35. (Contd.)

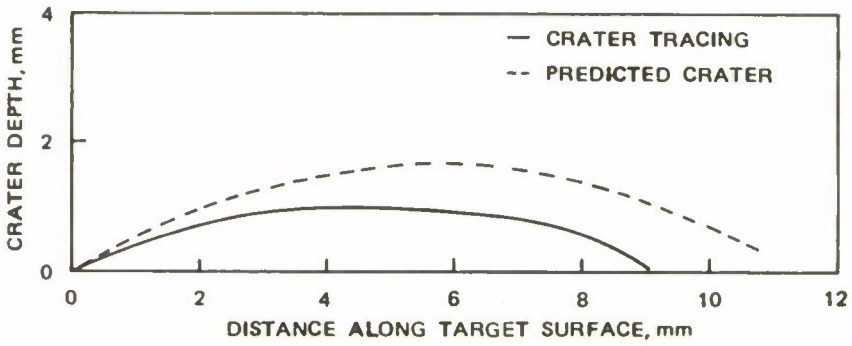

Impact speed, 0.373 km/s

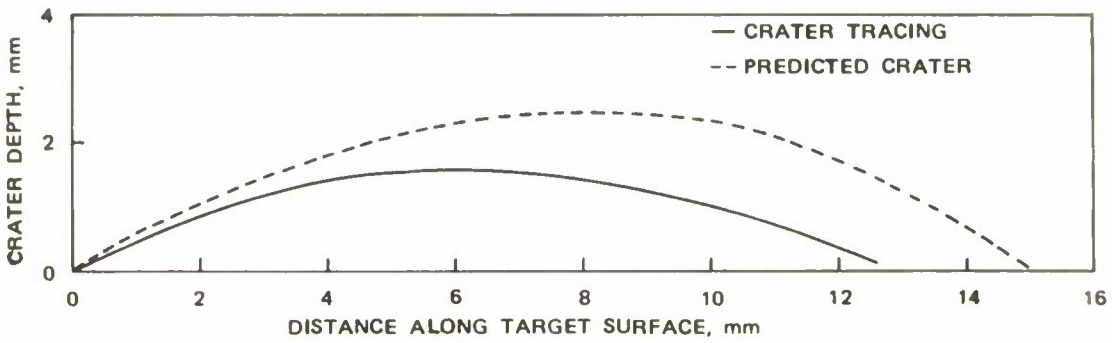

Impact speed, 0.522 km/s

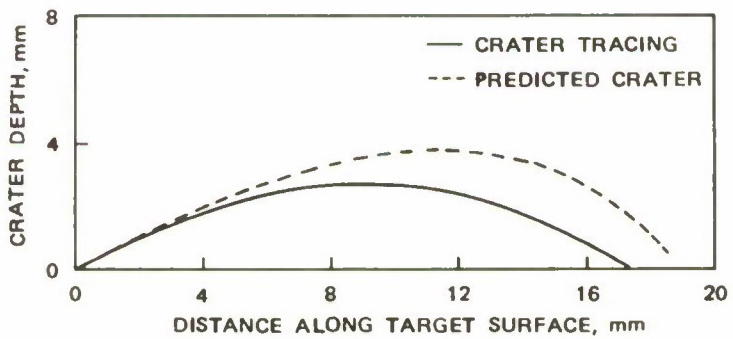

Impact speed, 0.729 km/s

FIGURE 36. Measured and Predicted Crater Shapes for Impact of a 6.35-mm Sphere at 60 Degrees Obliquity Against a 2024 Aluminum Alloy Plate of 6.35-mm Thickness and at Various Impact Speeds.

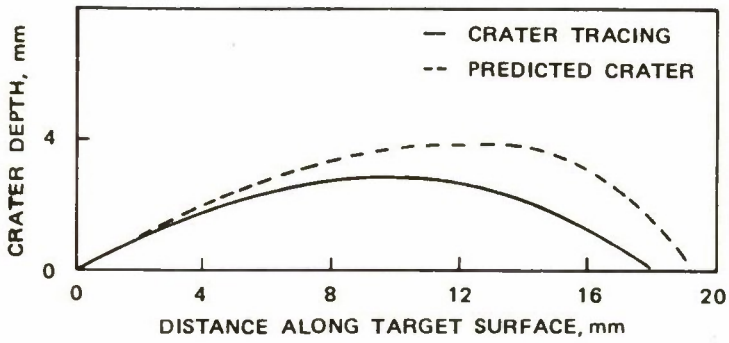

Impact speed, 0.752 km/s

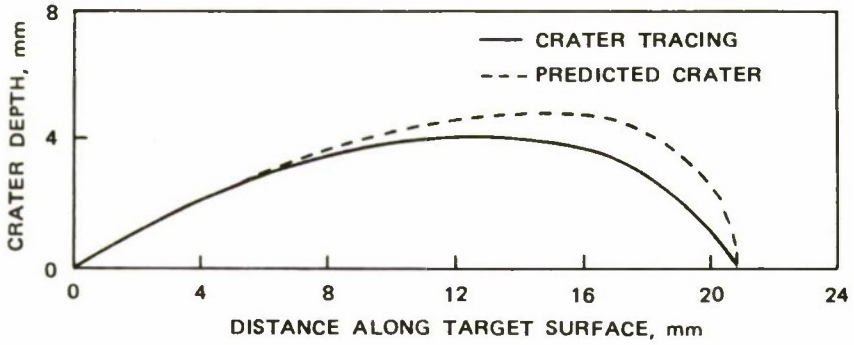

Impact speed, 0.901 km/s

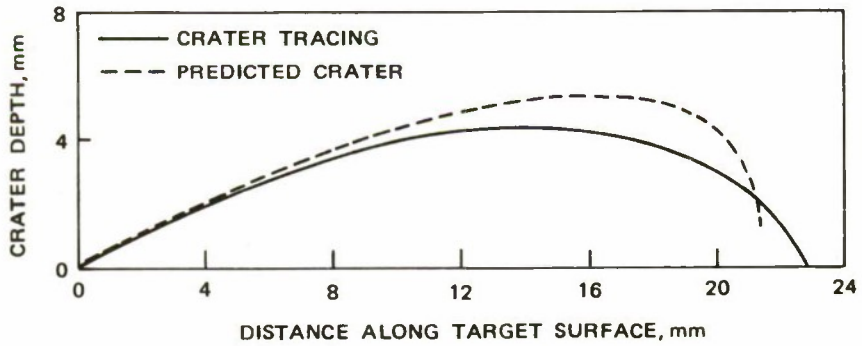

Impact speed, 0.966 km/s

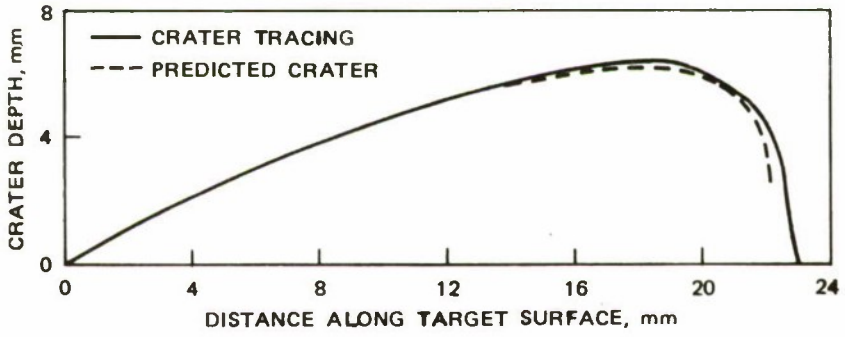

Impact speed, 1.062 km/s

FIGURE 36. (Contd.)

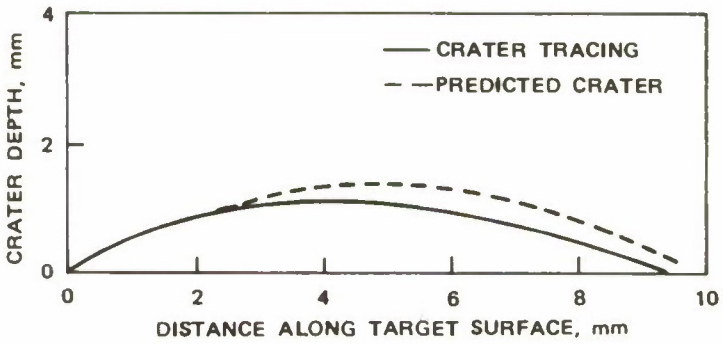

Impact speed, 0.331 km/s

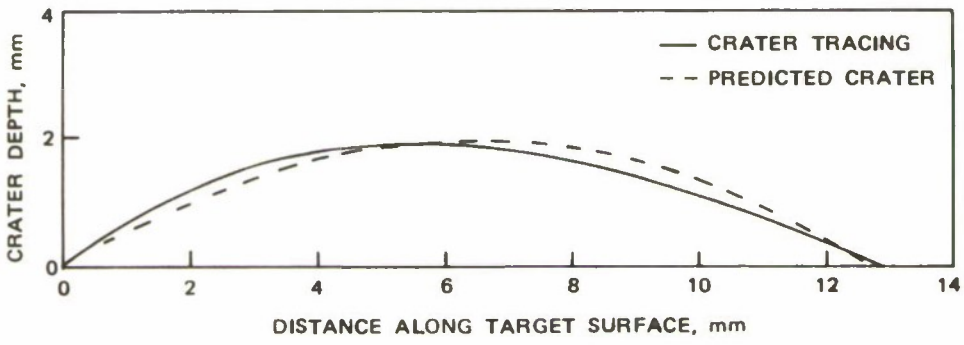

Impact speed, 0.446 km/s

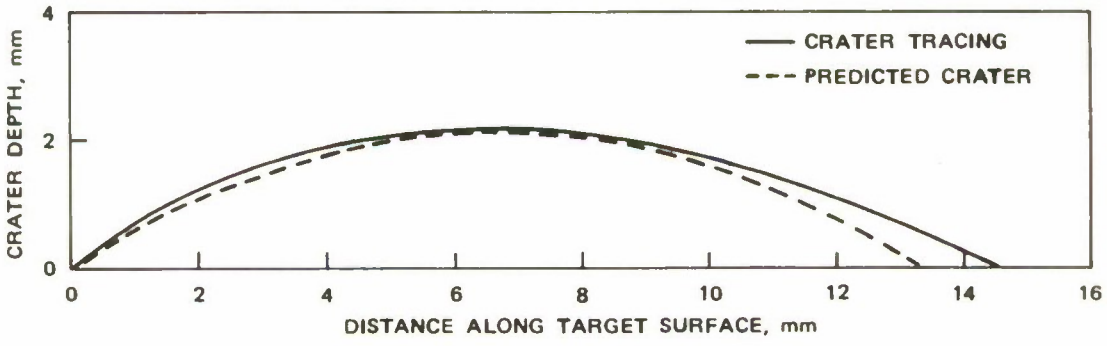

Impact speed, 0.474 km/s

FIGURE 37. Measured and Predicted Crater Shapes for Impact of a 6.35-mm Sphere at 60 Degrees Obliquity Against a 2024 Aluminum Alloy Plate of 3.18-mm Thickness and at Various Impact Speeds.

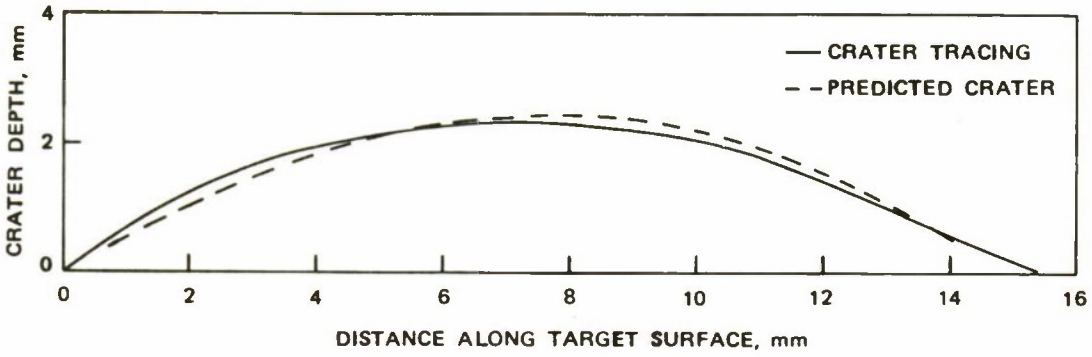

Impact speed, 0.538 km/s

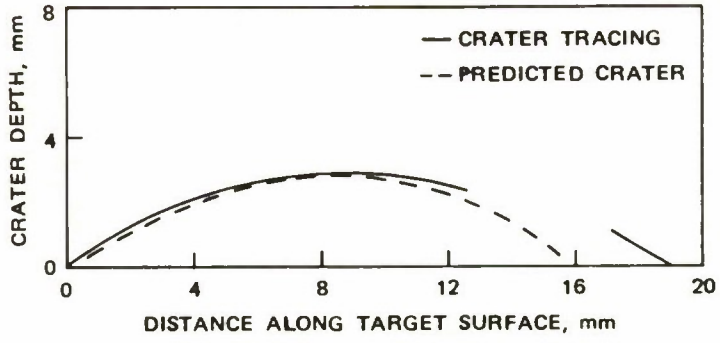

Impact speed, 0.597 km/s

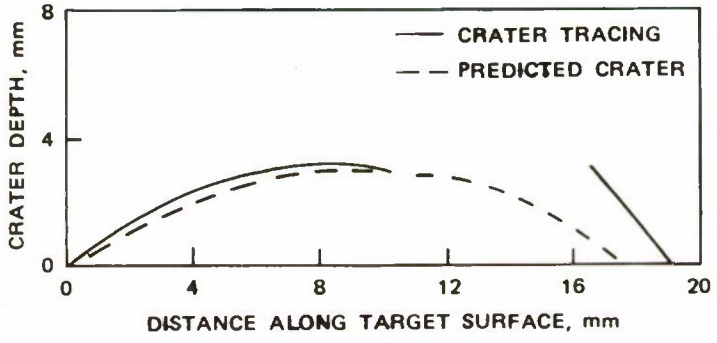

Impact speed, 0.644 km/s

FIGURE 37. (Contd.)

Figures 38 through 44 show the experimental data obtained for firings of 6.35-mm steel spheres against 1.47-mm-thick mild steel plates. In Figures 43 and 44 the solid line represents the predictions for 60-degree obliquity using the same value of P^* = 4.6 mm that was used in Figure 38 to fit the data at normal incidence. The data in both the ricochet and perforation ranges are widely discrepant with the prediction based on this value of P^*, and are seen to be fit better by the predictions using P^* = 3.0 and 3.8 mm, respectively, given by the dashed lines. Figures 41 and 42 show the experimental data for impact obliquities of 45 degrees, and predictions with P^* = 4.6 mm (solid lines), P = 3.5 mm (dashed lines, ricochet), and P^* = 4.4 mm (dashed lines, perforation). This shows that the simple model of ultimate failure of the plate using a constant value of P^* that did well for aluminum is poor for mild steel.

There are significant differences in the deformation and failure processes of mild steel and aluminum plates when impacted by steel spheres. These differences are potentially capable of explaining the degrees of conformity to the models proposed here. Figures 45 and 46 show cross sections of mild steel plates impacted by spheres. In the former, the plate has been deformed but not separated during a ricochet; in the latter, the plate has been deformed and a separation has been formed during an embedding impact. Figures 47 and 48 show external features of the corresponding impacts in aluminum targets. The mode of photography is not the same as for the steel targets because the overall failure process is quite different. This process consists of failures that radiate from the center of the crater (petaling). Note that the mild steel plate is extensively stretched and thinned in the ricochet impact, but the aluminum plate undergoes the complete failure of the petaling process. Thus it is clear that the failure processes in the mild steel target are much more prolonged, and apparently are not the simple deformations that are modeled by the formula for penetration resistance nor the complete failures modeled by the abrupt termination of resistance.

CONCLUSIONS

The agreement between experimental data and predictions at oblique incidence shows that the model of impact dynamics is reasonably accurate. Comparisons of crater measurements and analytical predictions show that the model of force during ricocheting impacts is a reasonable approximation, but that the approximation makes a systematic error that results in overprediction of crater length at low speeds and underprediction at higher speeds. (There are theoretical bases for expecting a high transient stress that is not included in the present model and that could account for the discrepancy.) Comparisons of experimental data with analytical predictions of the correlation of residual speed and obliquity with impact speed and obliquity show that failure of the plate has a distinct and identifiable effect on the correlation and that the form of modeling may be different for different materials.

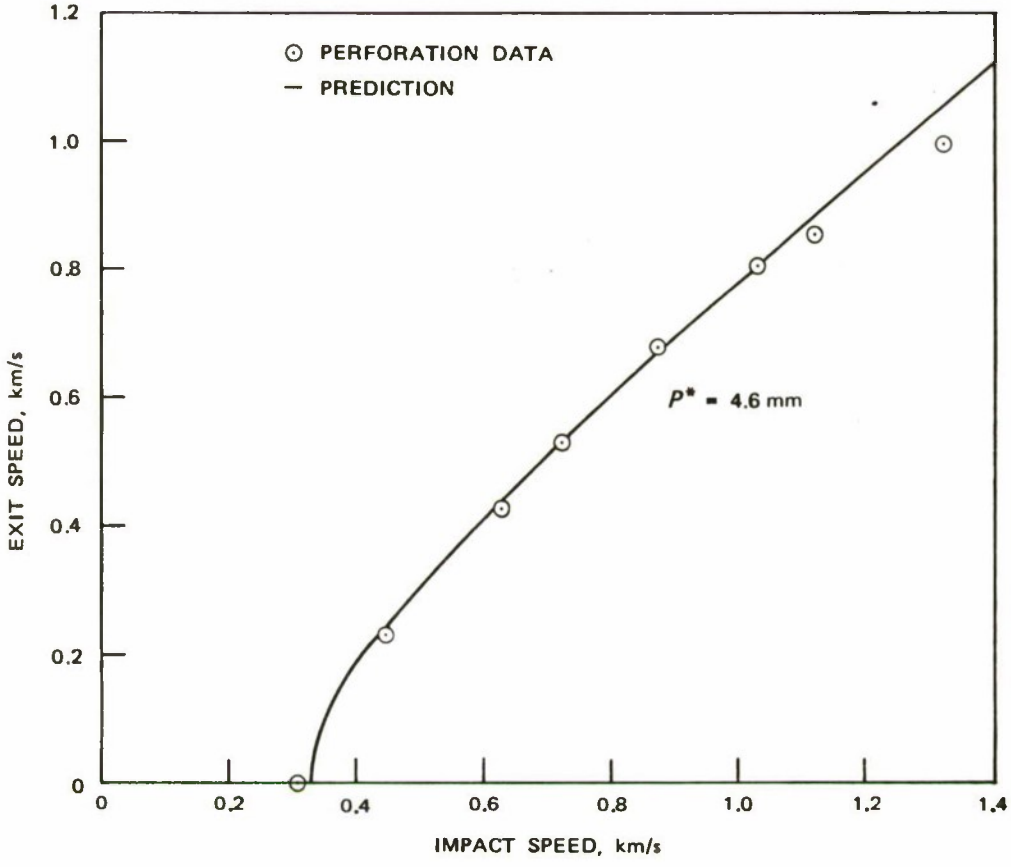

FIGURE 38. Data and Predictions of Exit Speeds for 6.35-mm Spheres Fired Against Mild Steel Targets of 1.47 mm Thickness and at Zero Degree Obliquity.

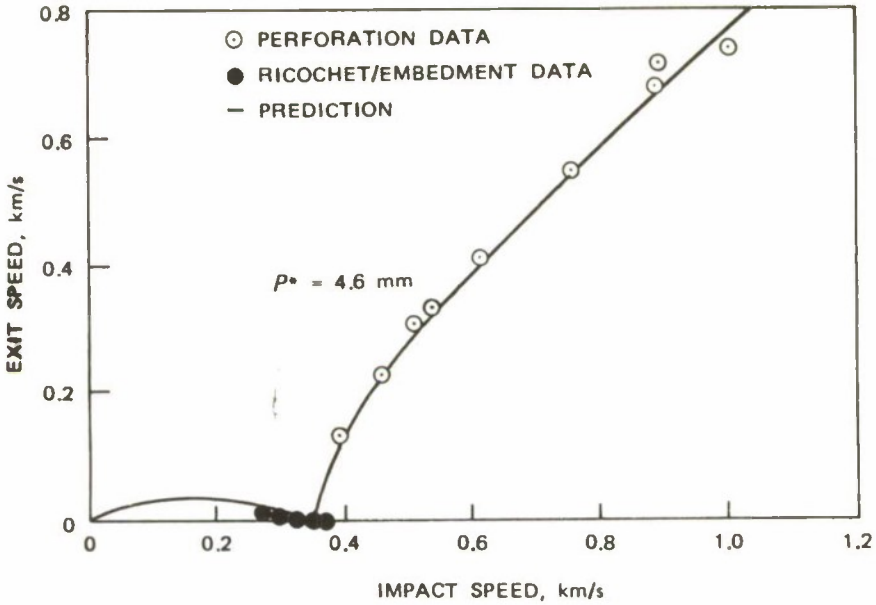

FIGURE 39. Data and Predictions of Exit Speeds for 6.35-mm Spheres Fired Against Mild Steel Targets of 1.47 mm Thickness and at 30 Degrees Obliquity.

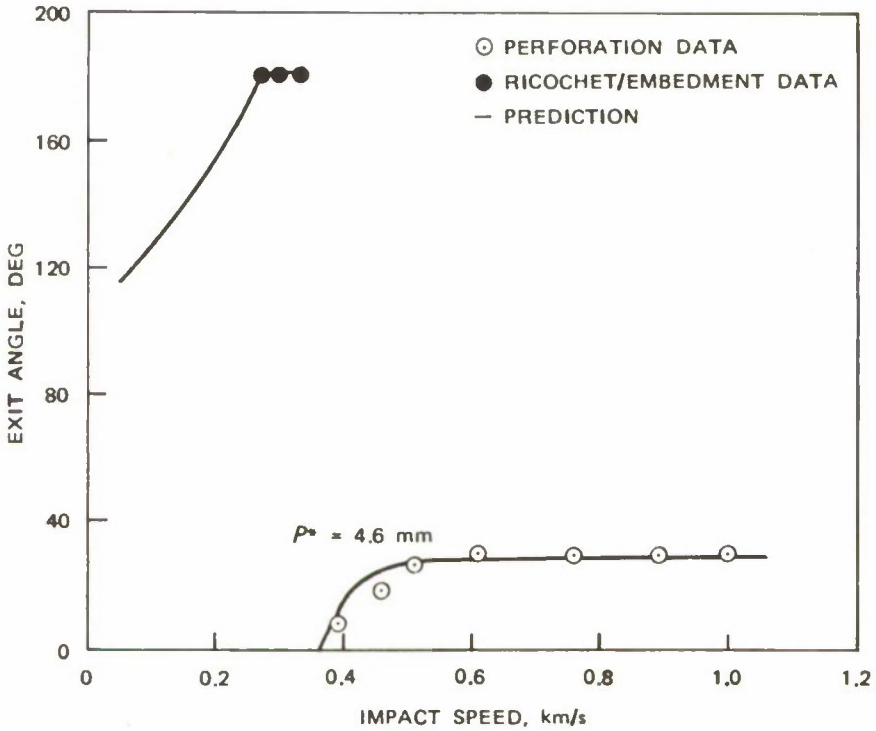

FIGURE 40. Data and Predictions of Exit Obliquities for 6.35-mm Spheres Fired Against Mild Steel Targets of 1.47 mm Thickness at 45 Degrees Obliquity.

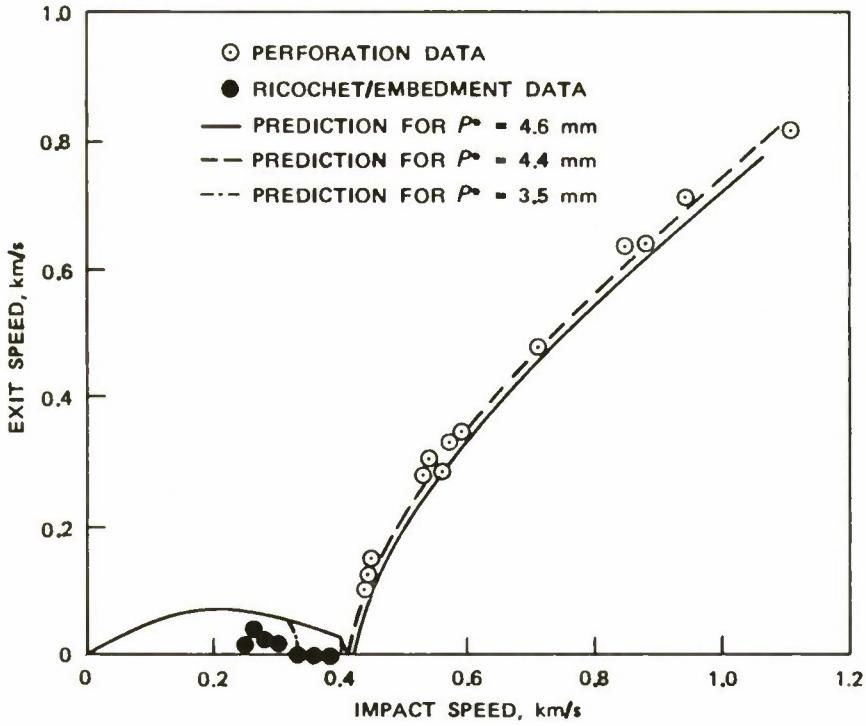

FIGURE 41. Data and Predictions of Exit Speeds for 6.35-mm Spheres Fired Against Mild Steel Targets of 1.47 mm Thickness and at 45 Degrees Obliquity.

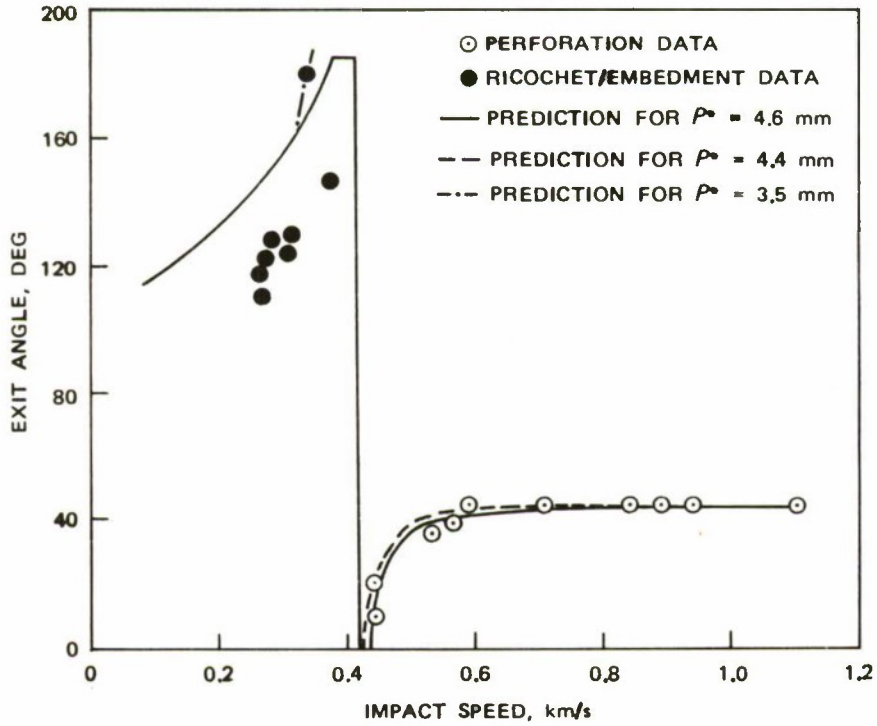

FIGURE 42. Data and Predictions of Exit Obliquities for 6.35-mm Spheres Fired Against Mild Steel Targets of 1.47 mm Thickness at 45 Degrees Obliquity.

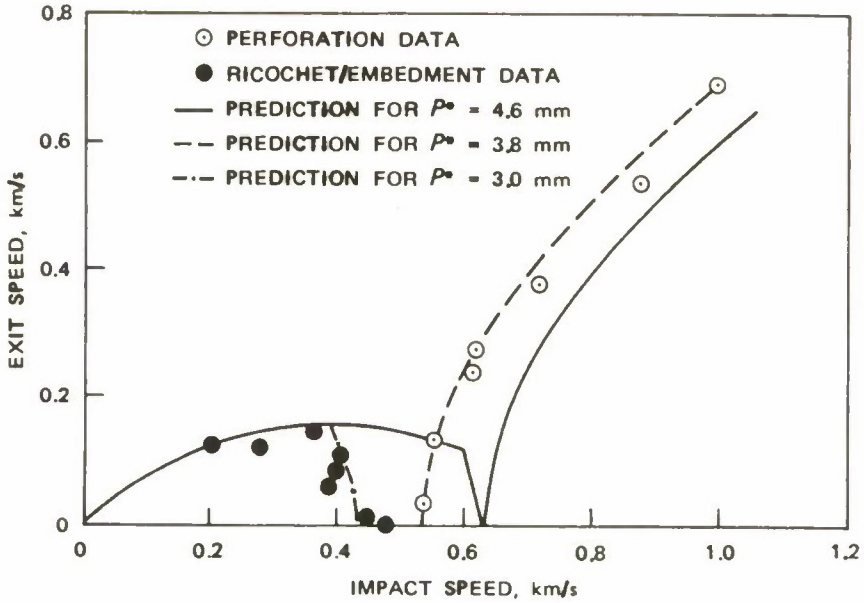

FIGURE 43. Data and Predictions of Exit Speeds for 6.35-mm Spheres Fired Against Mild Steel Targets of 1.47 mm Thickness and at 60 Degrees Obliquity.

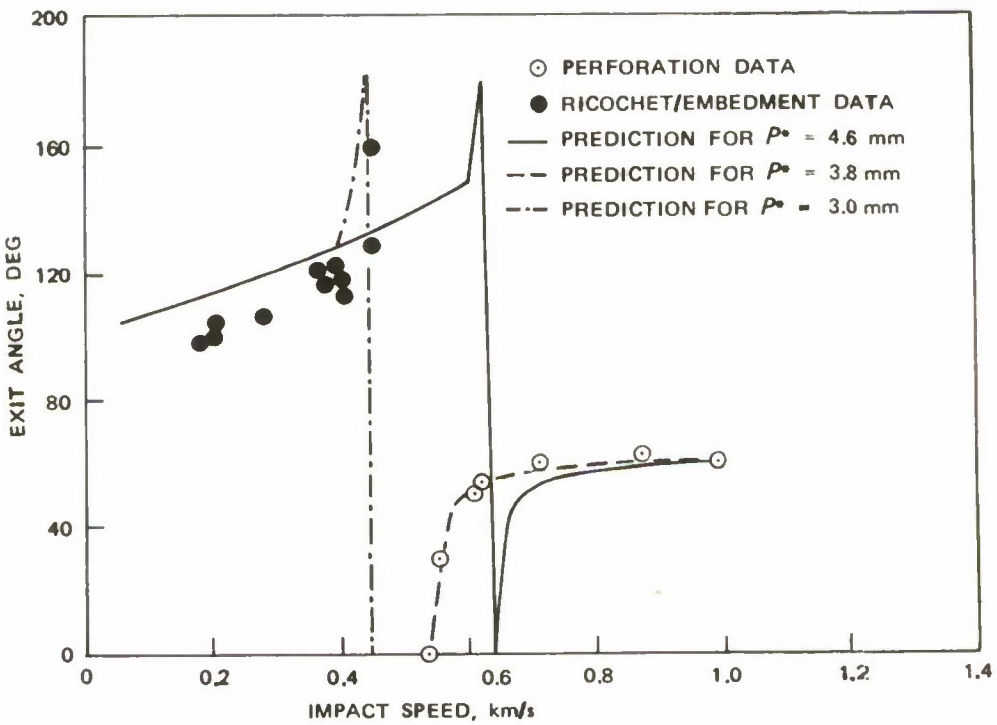

FIGURE 44. Data and Predictions of Exit Obliquities for 6.35-mm Spheres Fired Against Mild Steel Targets of 1.47 mm Thickness and at 60 Degrees Obliquity.

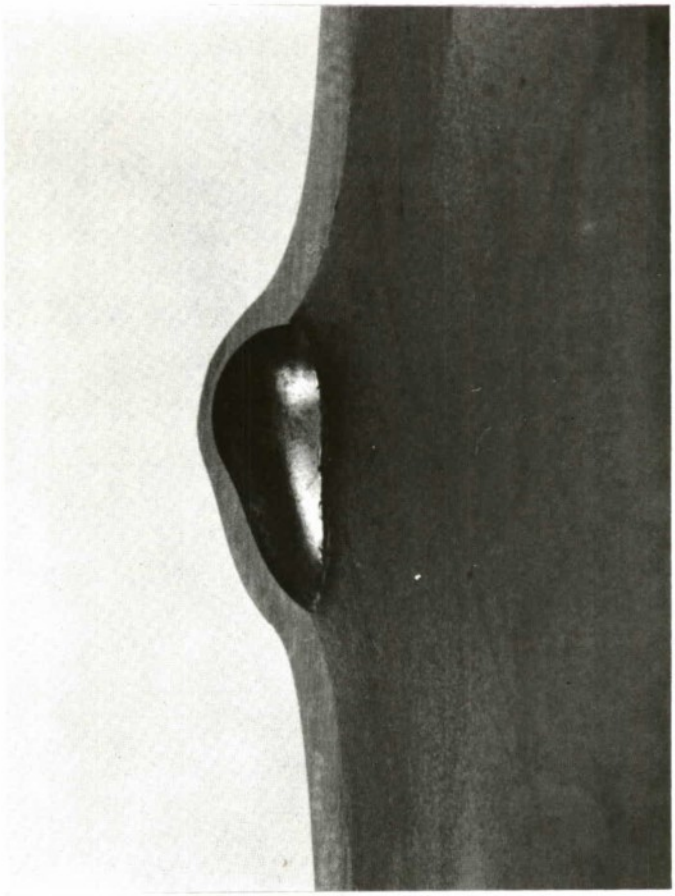

FIGURE 45. Cross Section of a Mild Steel Plate Impacted by a Ricocheting Sphere.

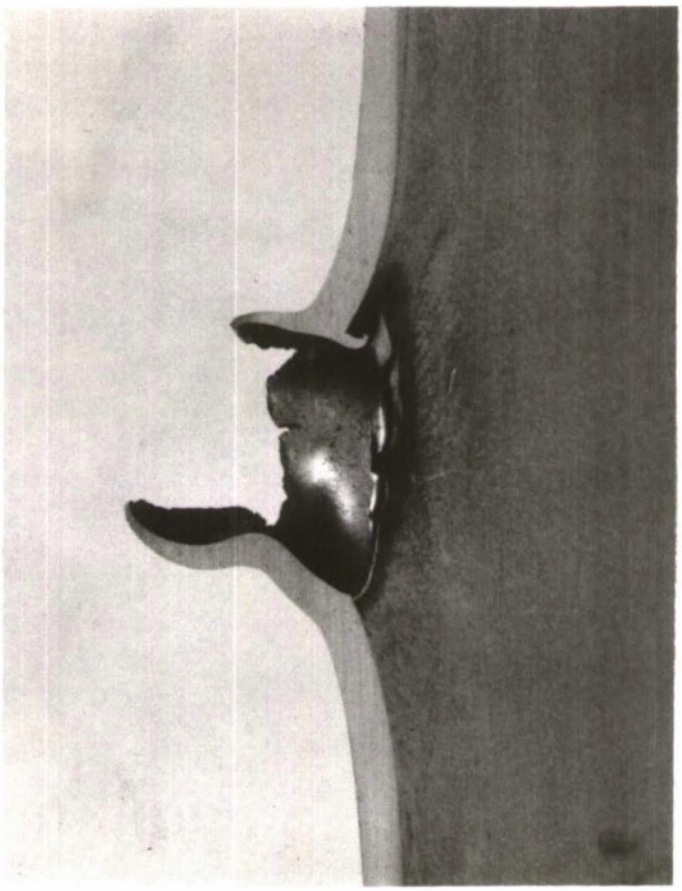

FIGURE 46. Cross Section of a Mild Steel Plate Impacted by an Embedding Sphere.

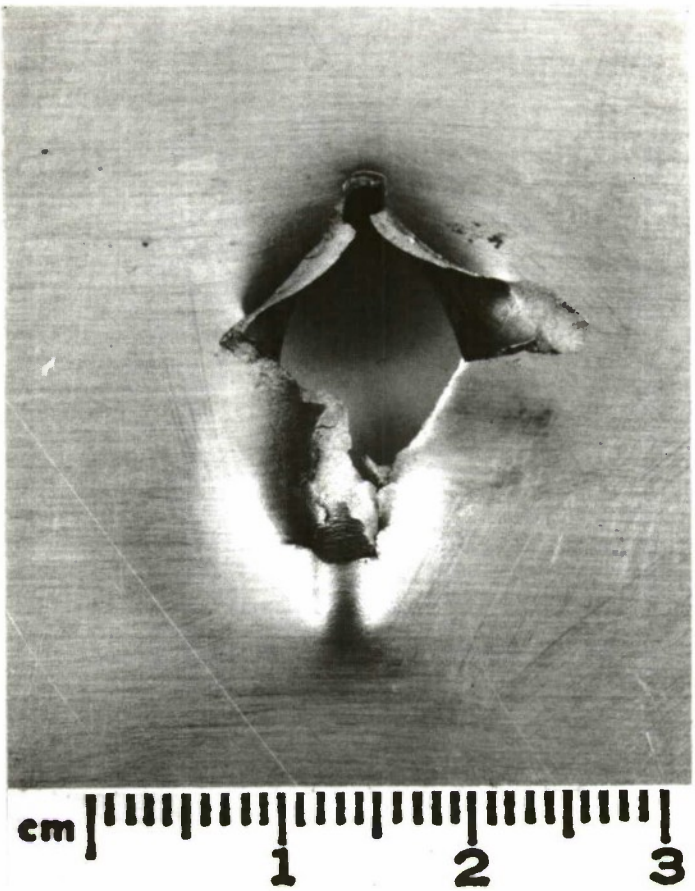

FIGURE 47. Exit Side View of the Deformation and Failure in a 2024 Aluminum Alloy Plate Caused by a Ricocheting Sphere.

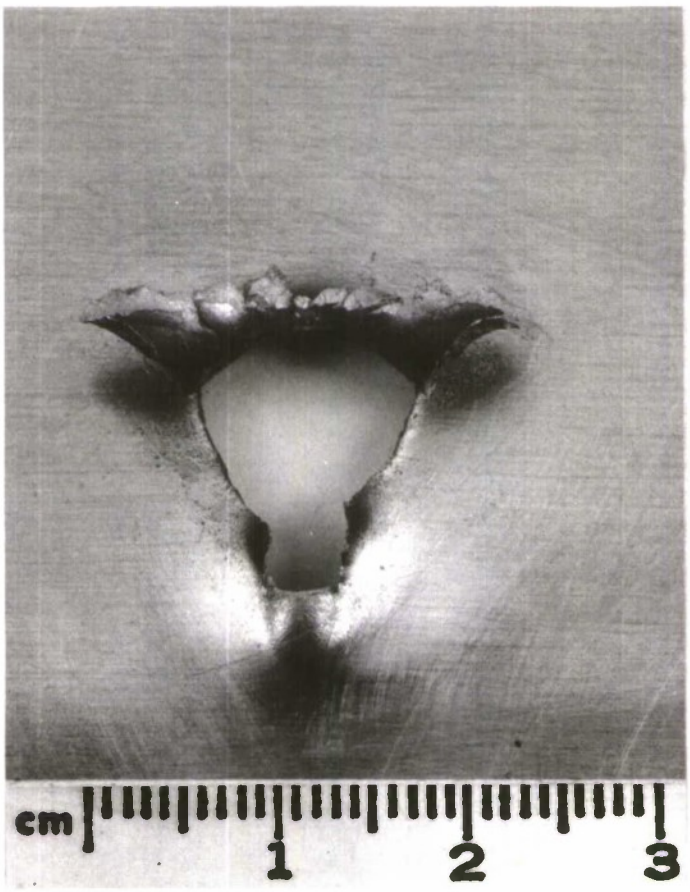

FIGURE 48. Exit Side View of the Deformation and Failure in a 2024 Aluminum Alloy Plate Caused by an Embedding Sphere.

Specific features of these correlations, the spike in the obliquity curves, and the precipitous drop in the speed curves are associated with failure processes in the plate. These features are supported by the experimental data, but are not clearly obvious without the analytical predictions.

The modeling of the force on the sphere without failure, and the modeling of failure and the effect of failure on impact dynamics are distinct processes in this investigation. The recognition of these distinct parts of impact dynamics and the role of material behavior in each should prove useful in interpreting further studies of the correlation of impact parameters, configuration of the impacting system, and material parameters with the final outcome of impact.

NOMENCLATURE

A	Presented area of the sphere in contact with the plate
B	Constant in least squares fit of residual-speed to impact-speed data
F	Force on the sphere
F', F''	Contributions to the force calculation
F_D	Component of force that decelerates the sphere
F_L	Component of force that deflects the sphere
M	Constant in the least square fit of residual-speed to impact-speed data
P	Penetration of the sphere beyond the front surface of the plate
P^*	Critical penetration beyond which the plate fails
R_e	Radius of embedment
R_s	Radius of the sphere
S	Distance along the trajectory of the sphere
T	Plate thickness
V	Speed of the sphere
V_s	Initial speed of the sphere
X	Coordinate of the trajectory
Y	Coordinate of the trajectory
a	Empirical constant in the calculation of force
b	Empirical constant in the calculation of force
d	Diameter of the projectile
h	Distance parameter in the calculation of the relief of force due to plugging
m	Mass of the sphere
r	Radius of curvature of the trajectory of the sphere
t	Time
x	Coordinate in the description of the shape of the crater
y	Coordinate in the description of the shape of the crater
Γ_e, Γ_s	Angles used in calculation of the presented area for oblique impact
Ω	Angle used to determine contact of the plate with the sphere
α^*	Angular parameter used to locate failure of the plate
β	Angular parameter used to determine the surface of the sphere that has no resisting force
θ	Angle of obliquity
θ_s	Initial obliquity of the trajectory
θ_1	Angle used in determining presented area after plate failure
ϕ	Angle between the force on the sphere and the normal to the plate
ψ	Angle between the sphere's line of flight and the normal to the contact surface

INITIAL DISTRIBUTION

1 Director of Navy Laboratories
13 Naval Air Systems Command
  AIR-30212 (2)
  AIR-350 (1)
  AIR-350D (1)
  AIR-5108 (1)
  AIR-5321 (1)
  AIR-5323 (2)
  AIR-5324 (1)
  AIR-53242 (1)
  AIR-533 (1)
  AIR-954 (2)
5 Chief of Naval Operations
  OP-03EG (2)
  OP-05 (1)
  OP-098 (1)
  OP-55 (1)
2 Chief of Naval Material
  MAT-03 (1)
  MAT-03PB (1)
7 Naval Sea Systems Command
  SEA-033 (5)
  SEA-09G32 (2)
4 Chief of Naval Research, Arlington
  ONR-102 (1)
  ONR-429 (1)
  ONR-461 (1)
  ONR-473 (1)
1 Air Test and Evaluation Squadron 5
1 Fleet Anti-Air Warfare Training Center, San Diego
1 Marine Air Base Squadron 32, Beaufort
1 Marine Corps Air Station, Beaufort
1 Naval Air Engineering Center, Philadelphia
1 Naval Air Force, Atlantic Fleet
2 Naval Air Force, Pacific Fleet
1 Naval Air Station, North Island
2 Naval Air Test Center, Patuxent River (Aeronautical Publications Library)
1 Naval Avionics Facility, Indianapolis (Technical Library)
1 Naval Explosive Ordnance Disposal Facility, Indian Head
1 Naval Ordnance Station, Indian Head (Technical Library)
1 Naval Postgraduate School, Monterey
1 Naval Ship Research and Development Center, Bethesda

5 Naval Surface Weapons Center, White Oak
  Code 242, Dr. Liddiard (1)
  Dr. S. Jacobs (1)
  J. Erkman (1)
  Guided Missile Warhead Section (1)
  Technical Library (1)
1 Naval Undersea Center, San Diego (Code 1311)
1 Office of Naval Research Branch Office, Chicago
1 Office of Naval Research Branch Office, Pasadena
1 Operational Test and Evaluation Force
1 Pacific Missile Test Center, Point Mugu (Technical Library)
1 Army Armament Command, Rock Island (SMUAP-MI-T, Technical Library)
1 Aberdeen Proving Ground (Development and Proof Services)
3 Army Ballistics Research Laboratories, Aberdeen Proving Ground
  AMXBR-T, Detonation Branch (1)
  AMXBR-XA-FI (1)
  AMXRD-AO, J. Sperrazza (1)
1 Army Research Office, Durham
4 Frankford Arsenal
  Pitman-Dunn Laboratory (3)
1 Harry Diamond Laboratories (Technical Library)
4 Picatinny Arsenal
  SARPA-AD--D-A-3, J. Pentel (1)
  Technical Library (3)
1 Radford Army Ammunition Plant
1 Redstone Arsenal (Rocket Development Laboratory, Test and Evaluation Branch)
1 Rock Island Arsenal
1 White Sands Missile Range (STEWS-AD-L)
1 Yuma Proving Grounds (STEYT-GTE (M&W Branch))
1 Tactical Air Command, Langley Air Force Base (TPL-RQD-M)
1 Air University Library, Maxwell Air Force Base
3 Armament Development & Test Center, Eglin Air Force Base
2 57th Fighter Weapons Wing, Nellis Air Force Base
  FWOA (1)
  FWOT (1)
3 Tactical Fighter Weapons Center, Nellis Air Force Base
  COA (1)
  CRCD (1)
  CTE (1)
12 Defense Documentation Center
1 Defense Nuclear Agency (Shock Physics Directorate)
1 Weapons Systems Evaluation Group
1 Langley Research Center (Technical Library)
1 Lewis Research Center
2 Allegany Ballistics Laboratory, Cumberland, Md.
2 Applied Physics Laboratory, JHU, Laurel, Md. (Document Library)
1 Arthur D. Little, Inc., Cambridge, Mass. (W. H. Varley)

2 Chemical Propulsion Information Agency, Applied Physics Laboratory, Silver Spring, Md.
1 IIT Research Institute, Chicago, Ill. (Document Librarian for Department M)
1 Jet Propulsion Laboratory, CIT, Pasadena, Calif. (Technical Library)
1 Los Alamos Scientific Laboratory, Los Alamos, N. Mex. (Reports Library)
1 Princeton University, Forrestal Campus Library, Princeton, N. J.
1 Stanford Research Institute, Poulter Laboratories, Menlo Park, Calif.
1 The Rand Corporation, Santa Monica, Calif. (Technical Library)
1 University of California, Lawrence Radiation Laboratory, Livermore, Calif.
1 University of Denver, Denver Research Institute, Denver, Colo.

NWC 372 805 C (9/76) 160